POLITECNICO MILANO 1863

SCUOLA DI INGEGNERIA INDUSTRIALE
E DELL'INFORMAZIONE

Direct Numerical Simulation of a Single Rising Bubble in a Confined Domain: Wall-Induced Effects and Predictive Modeling

Tesi di Laurea Magistrale in
Aeronautical Engineering - Ingegneria Aeronautica

Andrea D'Atri, 10713600

Advisor:
Prof. Giorgio Besagni

Co-advisors:
Prof. Marco Edoardo Rosti
Ing. Nicolò Varallo

Academic year:
2025-2026

Abstract: Understanding bubbly flows requires an accurate description of individual bubble dynamics, in terms of terminal velocity, shape and interfacial area. Building on the analysis of Belleri, 2025 for a rising bubble in an unbounded liquid domain, the present work extends the investigation to confined geometries, examining wall-induced effects on single-bubble dynamics. Direct numerical simulations were performed using the in-house Volume-of-Fluid-based code *Fujin*, developed at the Okinawa Institute of Science and Technology, to systematically investigate the underlying physical mechanisms and generate a comprehensive numerical dataset. The simulations span a wide range of Morton and Eötvös numbers ($10^{-11} \leq Mo \leq 10^{8}$ and $10^{-2} \leq Eo \leq 10^{3}$) and multiple confinement ratios (χ = 0.167, 0.25, 0.5 and 0.667). The results show that confinement induces a reduction of the bubble terminal velocity, which is more pronounced at low Eo and high Mo numbers. A correlation for the velocity retardation is proposed as a function of the Eötvös and Morton numbers and of the confinement ratio. Confinement is also shown to promote longitudinal elongation and an earlier onset of dimpled and skirted configurations, with trends depending on fluid properties. Novel correlations for the bubble aspect ratio and the bubble deformation factor are introduced, extending existing unbounded formulations to include confinement ratio. The wall-induced velocity reduction is physically interpreted by showing that confinement localizes viscous dissipation within the bubble–wall gap, altering the power balance that governs bubble rise and leading to a new equilibrium point.

Key-words: Bubble, Confinement, VOF, Terminal velocity, Aspect ratio, Interfacial area

1. Introduction

1.1. Framing the problem

Gas bubbles rising inside liquid-filled vertical pipes find several engineering applications (Legendre and Zenit, 2025), including bubble column reactors, multiphase systems that enable mass and heat transfer among different phases (Shah et al., 1982). Gas and liquid naturally interact, without the need for additional components, resulting in higher simplicity, compactness and reduced maintenance.

Nomenclature

Non-dimensional parameters

E	Bubble aspect ratio [–]
BDF	Bubble Deformation Factor [–]
χ	Confinement ratio [–]
χ_c	Critical confinement ratio [–]
Re	Reynolds number [–]
Eo	Eötvös number [–]
We	Weber number [–]
Ga	Galilei number [–]
Mo	Morton number [–]
Ta	Tadaki number [–]
N_D	Brest number [–]
μ_r	Viscosity ratio [–]
ρ_r	Density ratio [–]
C_D	Drag coefficient [–]
$U/U_{\chi=0}$	Velocity retardation [–]
ΔU	Variation of U relative to $U_{\chi=0}$ [%]
ΔE	Variation of E relative to $E_{\chi=0}$ [%]
$C(\chi)$	Confinement correction coefficient [–]

Dimensional parameters

U	Bubble terminal velocity [m/s]
F_B	Buoyancy force [N]
F_σ	Surface tension force [N]
F_μ	Viscous force [N]
F_i	Inertia force [N]
V_g	Bubble volume [m^3]
V_l	Liquid volume [m^3]
A	Interfacial area [m^2]
A_{eq}	Equivalent interfacial area [m^2]
d_{eq}	Equivalent diameter [m]
D_{pipe}	Pipe diameter [m]
μ_g	Gas phase dynamic viscosity [Pa·s]
μ_l	Liquid phase dynamic viscosity [Pa·s]
μ	Mixture dynamic viscosity [Pa·s]
ρ_g	Gas phase density [kg/m^3]
ρ_l	Liquid phase density [kg/m^3]
ρ	Mixture density [kg/m^3]
$\Delta\rho$	Liquid–gas density difference [kg/m^3]
σ	Surface tension [N/m]
k	Local curvature of the interface [1/m]
t	Time [s]
$\mathbf{u}$	Velocity vector [m/s]
$\mathbf{g}$	Gravity acceleration vector [m/s^2]
$\mathbf{f}_\sigma$	Volumetric surface tension force [N/m^3]
p	Pressure [Pa]
p'	Modified pressure [Pa]
P_B	Buoyancy power [W]
P_D	Viscous dissipation [W]
$\mathbf{S}$	Strain rate tensor [1/s]

Code symbols

H	Continuum color function
P	Three-dimensional surface function
β	Sharpness parameter [–]
d	Normalization parameter [–]
ϕ	Cell-averaged color function
$\mathbf{X}$	Spatial coordinate vector
δ	Interface delta function [–]

Subscripts

$_{\chi=0}$	Unconfined configuration
$_{model}$	Prediction from present model
$_{literature}$	Prediction from literature models

Owing to these features, such reactors are largely used in chemical, biochemical and energy industries, with applications including: production of synthetic fuels, wastewater treatment, CO_2 capture and oxygenation, hydrogenation and fermentation of organic compounds (Besagni et al., 2018; Rollbusch et al., 2015).

In bubble column reactors, global flow properties strongly influence mass and energy transfer and, consequently, the overall reactor efficiency. However, these macroscopic characteristics originate from the behavior of a large number of individual bubbles, in terms of their rise velocity, shape and interfacial area. In light of the above, understanding the underlying physics governing single bubble motion and deformation, as well as being able to predict the main quantities describing them, represents a necessary first step towards the proper design and optimization of the reactors.

Even at the single-bubble scale, the problem is inherently complex, as bubble dynamics arise from the strong coupling between the deformable interface and the balance of several competing physical mechanisms, namely buoyancy, surface tension, viscous stresses and inertial effects. The dynamics are characterized by a feedback mechanism: the force balance drives bubble deformation; then, the resulting change in shape alters the surrounding flow field, which in turn modifies the forces acting on the bubble.

Belleri, 2025 performed a comprehensive numerical investigation of a single rising bubble in unbounded conditions over a wide range of fluid properties, with the purpose of characterizing bubble terminal velocity and shape.
However, in practical applications, bubbles rarely rise in unbounded liquid domains; instead, they evolve in confined geometries and interact with solid boundaries, such as the walls of a reactor. The presence of confinement modifies the flow field surrounding the bubble, thereby altering the force balance, with the result that bubble terminal velocity, shape and interfacial area may significantly deviate from those observed under unconfined conditions. Accurately capturing these wall-induced modifications is essential for the development of more realistic models and ultimately for a more reliable reactor design.

The scope of the present work is to extend the study of Belleri, 2025 to include confined geometries and to assess the effects of walls on bubble dynamics and deformation. In particular, the study aims at proposing new predictive correlations for bubble terminal velocity, shape and interfacial area, valid over a wide range of fluid properties and confinement levels, by means of high-fidelity numerical simulations.
The work is organized as follows. After this outline, the Introduction continues by presenting the metrics adopted in the work, while Sec. 2 provides a review of the relevant literature. The numerical methodology and governing equations are described in Sec. 3. The results are presented and discussed in Sec. 4, focusing on confinement effects on bubble terminal velocity, shape and interfacial area. Finally, the main findings are summarized in Sec. 5.

1.2. Characterization parameters

To derive results and correlations that are independent of the problem scale, dimensionless numbers are adopted. They also quantify the relative significance of the forces governing the system, namely inertial (F_I), viscous (F_μ), surface tension (F_σ) and buoyancy (F_B) forces. The most commonly used are: Reynolds, Eötvös, Weber, Galilei and Morton numbers (Eq. (1a) to (1e)).

$$Re = \frac{F_I}{F_\mu} = \frac{d_{eq}\rho_l U}{\mu_l} \tag{1a}$$

$$Eo = \frac{F_B}{F_\sigma} = \frac{d_{eq}^2 \rho_l g}{\sigma} \tag{1b}$$

$$We = \frac{F_I}{F_\sigma} = \frac{d_{eq} U^2 \rho_l}{\sigma} \tag{1c}$$

$$Ga = \frac{F_B}{F_\mu} = \frac{\rho_l \sqrt{g\, d_{eq}^3}}{\mu_l} \tag{1d}$$

$$Mo = \frac{F_B {F_\mu}^4}{{F_I}^2 F_\sigma^3} = \frac{\Delta\rho\, \mu_l^4 g}{\rho_l^2 \sigma^3} \tag{1e}$$

where $\Delta\rho = \rho_l - \rho_g$ denotes the liquid–gas density difference.
The bubble length scale adopted in the definition of non-dimensional numbers is the equivalent diameter d_{eq}, defined as the diameter of a sphere having the same volume as the bubble:

$$d_{eq} = \sqrt[3]{\frac{6V_g}{\pi}} \tag{2}$$

This choice guarantees a physically relevant measure of bubble size for all possible bubble shapes.

In order to obtain quantitative results regarding bubble shape, metrics must be introduced. The most commonly adopted in literature are aspect ratio and bubble deformation factor.
The aspect ratio (E) is a non-dimensional parameter, defined as the ratio between the minor (a) and the major (b) axis of the bubble:

$$E = \frac{a}{b} \tag{3}$$

It is a quantitative indicator of the deviation from sphericity: spherical bubbles have $E = 1$, while ellipsoidal bubbles satisfy $0 < E < 1$, with smaller values corresponding to more elongated shapes. Aspect ratio plays a crucial role in describing bubble dynamics, as it quantifies the effect of shape on drag coefficient and terminal velocity (Moore, 1965; Rastello et al., 2011) and directly influences heat and mass transfer (Lochiel and Calderbank, 1964). However, E is meaningful only for fully convex shapes; it becomes inadequate for highly deformed configurations with concave interfaces, which cannot be described by the main axes.

The bubble deformation factor (BDF), is the ratio between the actual interfacial area of the bubble (A) and an equivalent area (A_{eq}), defined as the surface of a volume-equivalent sphere. Recalling Eq. (2), the diameter of this sphere is d_{eq}:

$$BDF = \frac{A}{A_{eq}} = \frac{A}{\pi d_{eq}^2} \tag{4}$$

Being the sphere the least interfacial area shape, any deviation from it result in a $BDF > 1$. Unlike the aspect ratio, the bubble deformation factor does not require full convexity and therefore remains meaningful for bubbles presenting concave regions or thin fluid layers, to which is particularly sensitive, yielding larger values. For this reason, BDF has been adopted in literature to characterize highly deformed bubble shapes (Cannon et al., 2024). Intuitively, for convex shapes the bubble deformation factor is inversely related to the aspect ratio (Wellek et al., 1966; Legendre et al., 2012). Since interphase transfer processes are primarily governed by the interfacial area, variations in bubble surface directly impact mass and energy transfer and, consequently, reactor efficiency (Maalej et al., 2003). Accordingly, the BDF is directly associated with reactor performance.

To understand the number of independent non-dimensional groups governing bubble dynamics and deformation, a dimensional analysis is performed (Bhaga, 1977). The relevant physical quantities influencing bubble motion are:

$$f(U, d_{eq}, \sigma, \mu_l, \mu_g, \rho_l, \rho_g, g) = 0 \tag{5}$$

However, in most cases of interest, the density and viscosity of the gas phase are significantly smaller than those of the liquid phase ($\mu_r << 1$, $\rho_r << 1$) and the terminal velocity was shown to be independent of viscosity (μ_r) and density (ρ_r) ratios by Belleri, 2025. These observations suggest simplifying Eq. (5) by neglecting ρ_g and μ_g, thereby reducing the number of governing parameters to six.
According to the Vaschy–Buckingham Π theorem, six variables involving three fundamental dimensions yield three dimensionless groups, two independent and one dependent. Among the possible combinations, the relation $f(Re, Eo, Mo) = 0$ is commonly adopted in literature to study the terminal velocity whereas $f(E, Eo, Re) = 0$ can be used to describe the shape.

In order to quantitatively account for confinement effects on bubble dynamics, a numerical indicator is introduced: the confinement ratio (χ). It is a non-dimensional parameter, defined as the ratio between the equivalent bubble diameter (d_{eq}) and a characteristic length of the reactor. Since most industrial reactors consist of pipes, a cylindrical geometry is assumed and the pipe diameter (D_{pipe}) is adopted as the representative length scale:

$$\chi = \frac{d_{eq}}{D_{pipe}} \tag{6}$$

2. Literature review

2.1. Drag coefficient and terminal velocity

A large number of studies have investigated the drag coefficient and terminal velocity of rising bubbles, leading to the development of numerous correlations based on dimensionless parameters.
One of the earliest and most cited contributions is Clift et al., 1978, who empirically correlated the bubble Reynolds number to the Eötvös and Morton numbers over a wide range of conditions. This led to the formulation of the "Grace diagram", an Eo–Re map with iso–Mo curves.
In parallel, theoretical studies sought analytical expressions for bubble drag coefficient. Among them: Hadamard, 1911 and Rybczynski, 1911 for $Re << 1$; Acrivos and Taylor, 1962 for $Re \leq 1$; Moore, 1963 for $Re \geq 50$ and Levich, 1962 for $Re >> 1$. However, these studies are mainly based on asymptotic formulations and limited to pure systems, strongly restricting their range of validity. Consequently, empirical and semi-empirical correlations were developed to cover intermediate Re, including: Ishii and Chawla, 1979 for $Eo < 16$; Grace, 1973 for $Eo < 40$ and $Mo < -3$.
Tomiyama et al., 1998 systematically collected available correlations to develop an analytical model for the drag coefficient, applicable over a wide range of fluid properties:

$$C_D = \max\left\{\min\left[\frac{16}{Re}(1 + 0.15Re^{0.687}), \frac{48}{Re}\right], \frac{8}{3}\frac{Eo}{Eo+4}\right\} \tag{7}$$

From this model, a correlation $f(Re, Eo, Mo) = 0$ was derived and used to construct an updated version of the Grace diagram, which is shown in Fig. 1 and is adopted in the present work.

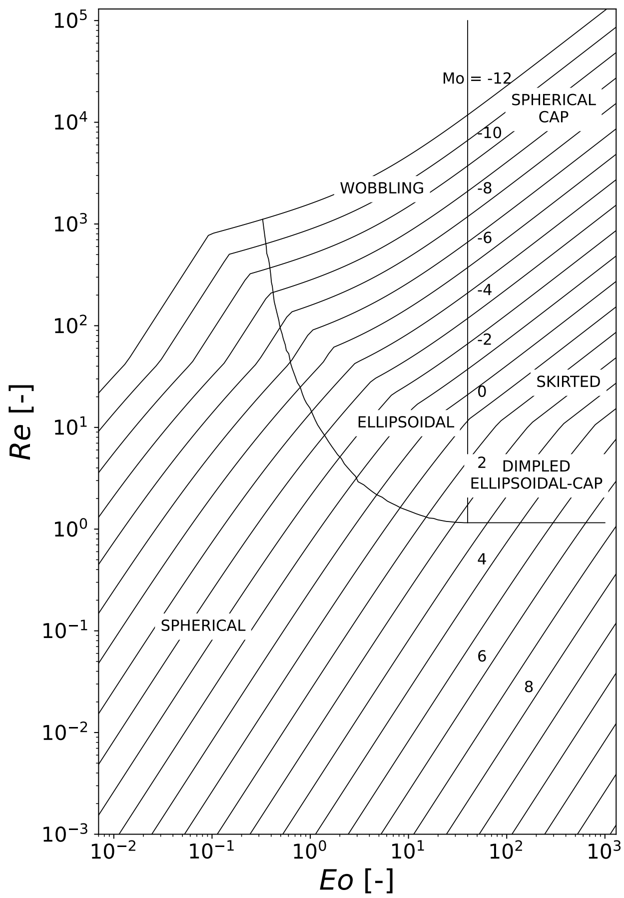

Figure 1: Grace diagram with bubble shape regimes, based on the formulation of Tomiyama et al., 1998 and the classification of Clift et al., 1978.

2.2. Shape regimes and deformation correlations

While numerous studies have addressed the bubble drag coefficient and terminal velocity, fewer have provided quantitative insights into bubble shape. Clift et al., 1978 identified three primary shape regimes (spherical, ellipsoidal and spherical-cap/ellipsoidal-cap), offered qualitative descriptions for their morphology and mapped the regions in the Grace diagram (Fig. 1) where each regime typically appears. Images of representative bubbles for all shape regimes are provided in Fig. 2.

1) *Spherical regime*: bubbles exhibit a shape closely approximated by a sphere (Fig. 2a). This occurs when surface tension and/or viscous forces dominate over inertia (low Eo and/or low Re). In fact, surface tension tends to minimize the interfacial area, maintaining a spherical shape, while viscosity damps any tendency to deform or oscillate.

2) *Ellipsoidal regime*: bubbles assume an oblate ellipsoidal geometry, with the minor axis aligned with the rising direction (Fig. 2b). This regime appears for intermediate Eo and Re, where inertial forces promoting deformation perpendicular to the direction of motion become comparable to surface tension and viscous forces. For high Re, inertia forces become dominant over viscous forces, which are no longer able to prevent periodic oscillations, leading to the development of a wobbling behavior in both bubble shape and trajectory. (Fig. 2e).

3) *Spherical-cap or ellipsoidal-cap regime*: bubbles exhibit a flatter rear interface and loose fore and aft symmetry. This behavior is characteristic of high Re and high Eo conditions, where interfacial forces are particularly low. For intermediate Re, a thin layer of fluid extending at the back of the bubbles develop, usually referred as skirt. Bubbles presenting this behavior are called dimpled ellipsoidal (Fig. 2c) and skirted (Fig. 2d).

However, Clift et al., 1978 defined regime boundaries only empirically, without providing analytical expressions. To obtain quantitative results, relations including aspect ratio and bubble deformation factor need to be formulated.

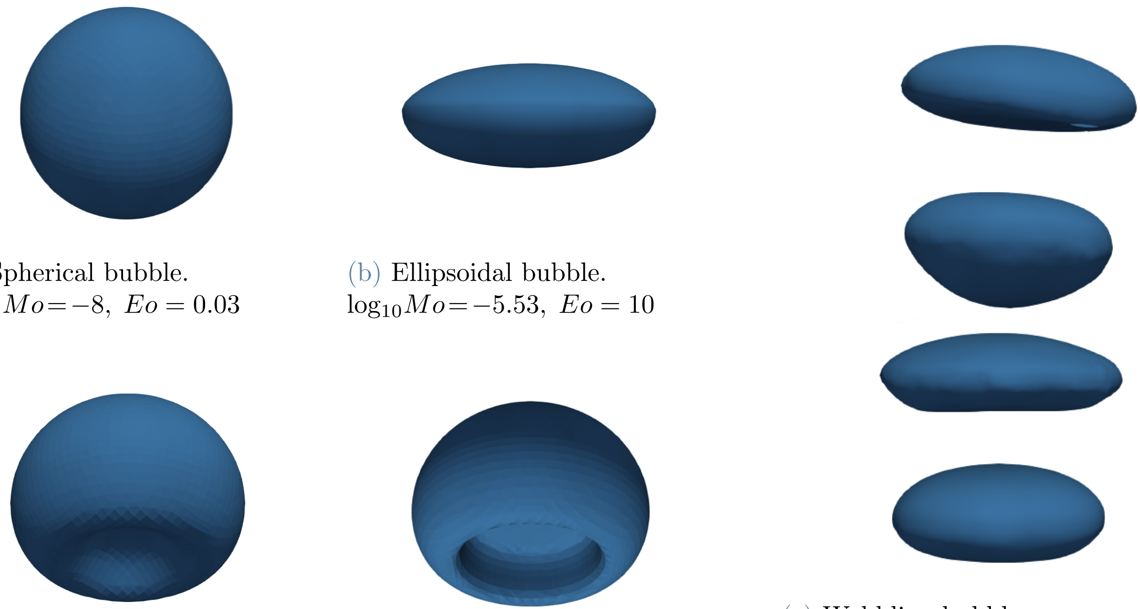

(a) Spherical bubble. $\log_{10}Mo{=}-8,\ Eo = 0.03$

(b) Ellipsoidal bubble. $\log_{10}Mo{=}-5.53,\ Eo = 10$

(c) Dimpled ellipsoidal bubble. $\log_{10}Mo{=}4,\ Eo = 300$

(d) Skirted bubble. $\log_{10}Mo{=}5,\ Eo = 1000$

(e) Wobbling bubble. $\log_{10}Mo{=}-11,\ Eo = 10$

Figure 2: Bubble shape regimes.

Several studies have attempted to correlate aspect ratio with non-dimensional groups. A fundamental reference in this context is the work of Wellek et al., 1966, who proposed the following general correlation:

$$E = \frac{1}{1 + \alpha_0 \Pi_{i=1}^{n_{tot}} \theta_i^{\alpha_i}} \tag{8}$$

with θ_i representing the relevant non-dimensional groups and α_0, α_i fitting coefficients determined through statistical analysis. They showed that a single group, specifically We, was sufficient to obtain a reasonably accurate correlation. Subsequently, several studies adopted this formulation based on a single parameter, including: Okawa et al., 2003 and Besagni and Inzoli, 2016, who correlated E to Eo; Moore, 1965 and Sugihara et al., 2007, who adopted We. However, these analysis considered low viscosity fluids (low Mo), where viscous forces do not have significant impact on the physical behavior.

Aoyama et al., 2016 and Besagni and Deen, 2020 pointed out that a general correlation spanning a wide range of Mo must account for all relevant forces acting on the bubble and therefore involve a combination of F_I, F_B, F_μ and F_σ. Accordingly, as shown by the dimensional analysis, two independent non-dimensional groups are required. Several combinations have been proposed: Tadaki and Maeda, 1961 introduced Tadaki number $Ta = ReMo^{0.23}$, which has largely been adopted in literature (Fan and Tsuchiya, 1990, Myint et al., 2007). However, Aoyama et al., 2016 showed that Ta weakly accounts for viscosity and therefore fails at large Mo, prompting the introduction of $Eo^{1.12}Re$. Besagni and Deen, 2020 considered the combination $EoRe$, which was subsequently adopted by Belleri, 2025, who derived the following correlation:

$$E = \frac{1}{[1 + 0.02EoRe]^{0.18}} \tag{9}$$

Far fewer studies have attempted correlations for the bubble deformation factor, mainly due to the challenges associated with experimental measurements of interfacial area. Among them, Mei and Cheng, 2022 and Mei and Cheng, 2024 who correlated BDF to Eo and Ga. Belleri, 2025 showed that the BDF is governed by the non-dimensional combination We^2/Eo, obtaining the relation:

$$BDF = 1.06 + 0.86(We^2/Eo) \tag{10}$$

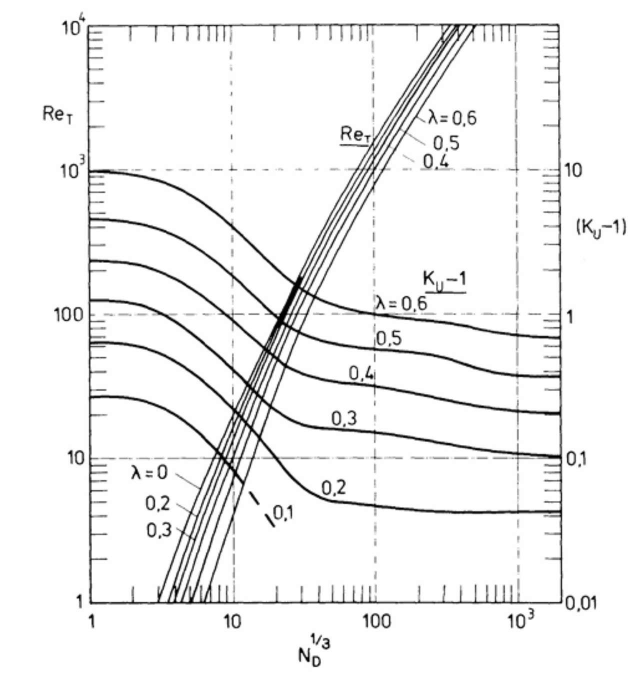

Figure 3: Graphical method from Clift et al., 1978 to predict velocity retardation ($1/K_U$) and Re for different values of χ, as a function of $N_D^{1/3}$.

2.3. Confinement effect

The presence of solid boundaries modifies the local flow field and the wake structure, thereby altering the force balance governing bubble motion and deformation. As a consequence, terminal velocity, aspect ratio and bubble deformation factor deviate from those observed in unconfined conditions and therefore more realistic correlations must include the influence of the wall.
Several studies have examined confinement effects on bubble dynamics, primarily focusing on fundamental wall-induced mechanisms acting on individual bubbles, while systematic investigations spanning a wide range of container sizes and aimed at establishing predictive correlations remain limited. Moreover, most studies addressed terminal velocity and lateral migration rather than bubble deformation, with the resulting correlations often limited to narrow ranges of fluid properties.

It is well established that increasing confinement leads to a reduction of the terminal velocity, a result that has been repeatedly confirmed across different theoretical and experimental works. Uno and Kintner, 1956 introduced the concept of velocity retardation, defined as the ratio between the terminal velocity in a confined geometry (U) and its unconfined counterpart ($U_{\chi=0}$); implicitly assuming that the influence of the walls can be expressed as a correction to $U_{\chi=0}$. Subsequently, numerous expressions for the velocity retardation were proposed and comprehensive reviews were provided by Bhaga, 1977 and Clift et al., 1978. Based on the Reynolds and Eötvös numbers, four dynamical regimes were identified:
1) $Re < 1$: the velocity retardation was theoretically derived by Haberman and Sayre, 1958:

$$\frac{U}{U_{\chi=0}} = \frac{1}{Re_{\chi=0}} \left(\frac{1+\mu_r}{2+3\mu_r} \right) \frac{1}{6K_h} \sqrt{\frac{Eo^3}{Mo}} \quad \text{(valid for: } \chi \leq 0.5\text{)}$$
$$K_h(\chi, \mu_r) = \frac{1 + 2.2757 \left(\frac{1-\mu_r}{2+3\mu_r}\right) \chi^5}{1 - 0.7017 \left(\frac{2+3\mu_r}{1+\mu_r}\right) \chi + 2.0865 \left(\frac{\mu_r}{1+\mu_r}\right) \chi^3 + 0.5689 \left(\frac{2-3\mu_r}{1+\mu_r}\right) \chi^5 - 0.72603 \left(\frac{1-\mu_r}{1+\mu_r}\right) \chi^6} \tag{11}$$

2) $1 < Re < 200$ and $Eo < 40$: Clift et al., 1978 provided a graphical method to estimate confinement-induced velocity reduction (Fig. 3). In this formulation, the velocity retardation is given by $1/K_U$ and can be directly obtained from the chart for different values of χ, together with the unconfined Reynolds number, as a function of $N_D^{1/3}$, where $N_D = 4/3Ga^2$ indicates the Brest number. Curves are only available for $\chi < 0.6$, thus limiting the applicability of this method.

3) $Re > 200$ and $Eo < 40$: Clift et al., 1978 proposed the correlation:

$$\frac{U}{U_{\chi=0}} = \sqrt{(1-\chi^2)^3} \quad \text{(valid for: } \chi \leq 0.6) \tag{12}$$

4) $Re > 1$ and $Eo > 40$: the effect of confinement was described by Collins, 1967 and Wallis, 1969:

$$\frac{U}{U_{\chi=0}} = 1.13e^{-\chi} \quad \text{(valid for: } 0.125 \leq \chi \leq 0.6) \tag{13}$$

Above a critical confinement ratio (χ_c), a significantly different dynamical behavior emerges: the terminal velocity becomes independent of χ and the bubble tends to adopt a bullet-like shape, commonly referred to as Taylor bubble (Davies and Taylor, 1950). The value of χ_c depends sensitively on fluid properties: $\chi_c \simeq 0.6$ for an air-water system (Nakahara and Tomiyama, 2003), $\chi_c \simeq 1$ for highly viscous liquid-liquid systems (Coutanceau and Texier, 1986). Classical velocity retardation correlations (Eq. (11) to (13)) restricted their range of validity to $\chi < 0.5$–0.6. Kurimoto et al., 2013 extended these studies to $\chi > 0.6$, proposing a classification criterion based on the drag coefficient. The bubble is considered to exhibit Taylor-like behavior when the Taylor-type drag coefficient (C_{DT}) becomes smaller than the particle-based drag coefficient (C_{DP}):

$$\text{Bubble behavior} = \begin{cases} \text{Particle-like}, & \chi \leq 0.6, \\ \text{Particle-like}, & \chi > 0.6 \text{ and } C_{DT} \geq C_{DP}, \\ \text{Taylor-like}, & \chi > 0.6 \text{ and } C_{DT} < C_{DP}. \end{cases} \tag{14}$$

Crucially, they showed that as long as the bubble exhibits a particle-like behavior, velocity retardation models given by Eq. (11) to (13) are still sufficiently accurate.
C_{DT} is modeled according to Hayashi et al., 2010:

$$\begin{gathered} C_{DT} = \frac{4}{3}\frac{\chi}{Fr_D^2} \qquad Fr_D = \sqrt{\frac{G\,H}{H/0.35^2 + F}} \\ F = \frac{1}{Re_D}\left(1 - 0.05\sqrt{Re_D}\right) \qquad G = \left(1 + \frac{3.87}{Eo_D^{1.68}}\right)^{-18.4} \qquad H = 0.0025\,[3 + G] \end{gathered} \tag{15}$$

where Re_D and Eo_D are the Reynolds and the Eötvös numbers respectively, defined using the pipe diameter as characteristic lenght scale.
The particle-based drag coefficient is instead evaluated as: $C_{DP} = \max(C_{DP}^{\mu}, C_{DP}^{\sigma i})$.
C_{DP}^{μ} is modeled according to Hayashi and Tomiyama, 2009:

$$\begin{gathered} C_{DP}^{\mu} = \frac{8}{Re}\left(\frac{2 + 3\mu_r}{1 + \mu_r}\right)(K_h + K_{ls} - 1) \\ K_{ls} = 1 + 0.15 Re_{\chi=0}^{0.687} \quad K_h\text{: defined in Eq. (11)} \end{gathered} \tag{16}$$

Finally, $C_{DP}^{\sigma i}$:

$$C_{DP}^{\sigma i} = \frac{8}{3}\frac{Eo}{Eo + 4}(1 - \chi^2)^{-3} \tag{17}$$

In addition to its impact on the terminal velocity, confinement has a profound influence on bubble shape. The experimental investigation of Bhaga, 1977 showed that increasing confinement progressively limits the lateral extension of the bubble and promotes elongation along the direction of gravity; with the extent of this deformation depending on the fluid properties and on the bubble equivalent diameter.
Moreover, confinement was shown to promote the formation of liquid skirt at the bubble rear, leading to an earlier onset of skirted and dimpled ellipsoidal shapes compared to unconfined conditions.
Although these wall-induced effects directly influence aspect ratio and bubble deformation factor, no correlations accounting for confinement effect are currently available, thereby motivating the purpose of the present study.

3. Numerical Model

3.1. Numerical framework

The investigation is carried out using Direct Numerical Simulation (DNS), in which the full Navier-Stokes equations are solved, without introducing turbulence modelling and without spatial and temporal filtering or averaging. Although computationally expensive, DNS is required to accurately capture small-scale interfacial mechanisms governing bubble dynamics, such as highly localized pressure gradients and strong interfacial curvature variations. (Esmaeeli and Tryggvason, 1998; Tryggvason et al., 2006). Additionally, in the low and intermediate Reynolds number regime considered here, no large-scale turbulence develops; instead, wake and wall interactions are dominated by small-scale motions (Popinet, 2009).

To perform the simulations, the Volume of Fluid method (VOF) has been employed (Hirt and Nichols, 1981). It is an interface-capturing technique, in which the interface is not tracked by a deformable mesh, but identified through the iso-contours of a scalar function that distinguishes the two fluids. Consequently, it is a fully Eulerian approach based on a fixed mesh, thus providing robustness, efficient parallelization and making the method particularly suitable for highly deformable bubbles and breakup phenomena. However, interface-capturing methods require solving an advection equation for the scalar field, which introduces numerical diffusion and thus smooths the interface, reducing the accuracy.
In the VOF method, the scalar function is the color function H, which indicates the fraction of the cell volume occupied by the gas phase. Therefore, $H = 1$ in cells entirely filled with gas phase, $H = 0$ where only liquid phase is present, $0 < H < 1$ in cells cut by the interface. Since H is purely advected, VOF automatically enforces volume conservation and therefore mass conservation in incompressible flows. Numerical solution of the advection equation requires geometrical reconstruction of the interface and computation of numerical fluxes. Different strategies have been proposed to these purposes, including the SLIC method by Noh and Woodward, 1976 and the PLIC method by Youngs, 1982. Comprehensive reviews can be found in Scardovelli and Zaleski, 1999 and Mirjalili et al., 2017.

Xiao et al., 2005 proposed Tangent of Hyperbola for Interface Capturing method (THINC), a variant of the VOF in which the color function is no longer a scalar quantity, but is reconstructed inside each cell as a continuous function having a step-like profile, specifically a hyperbolic tangent. This formulation enables an analytical calculation of numerical fluxes, normals and curvatures, avoiding explicit geometric reconstruction and reducing numerical diffusion, thereby preserving a sharper interface.
The original THINC was essentially one-dimensional, as the reconstruction was performed one spatial direction at a time. Ii et al., 2012 extended the method to fully multi-dimensional formulation (MTHINC) by reconstructing the hyperbolic tangent profile along the local interface normal, allowing the representation of more complex interface geometries.

Rosti et al., 2019 provided an advanced, stable and efficient version of MTHINC, which has been implemented in the in-house code *Fujin*, developed by the Complex Fluids and Flows unit at the Okinawa Institute of Science and Technology. *Fujin* is adopted to perform the simulations in the present work.

3.2. Governing Equations

The continuum color function $H(\mathbf{X})$ is defined within each cell as:

$$H(\mathbf{X}) = \frac{1}{2}\left[1 + \tanh\left(\beta(P(\mathbf{X}) + d)\right)\right] \tag{18}$$

where β is a sharpness parameter, d is a normalization parameter and $P(\mathbf{X})$ is a three-dimensional surface function. Let $\phi(\mathbf{X})$ be the cell-averaged value of H and $\mathbf{u}(\mathbf{X})$ the one-field velocity, the following advection equation can be written:

$$\frac{\partial \phi}{\partial t} + \nabla \cdot (\mathbf{u}H) = \phi \nabla \cdot \mathbf{u} \tag{19}$$

At each time step, Eq. (19) is solved numerically adopting a directional splitting approach followed by the imposition of the divergence-free condition. Once ϕ is known, the incompressible flow equations are solved. Here they are introduced in the one-fluid formulation:

$$\begin{cases} \rho\Big(\dfrac{\partial \mathbf{u}}{\partial t} + \nabla\cdot(\mathbf{u}\otimes\mathbf{u})\Big) = -\nabla p + \nabla\cdot\big[\mu(\nabla\mathbf{u}+\nabla\mathbf{u}^T)\big] + \mathbf{f}_\sigma + \rho\,\mathbf{g} \\ \nabla\cdot\mathbf{u} = 0 \end{cases} \tag{20}$$

The mixture density (ρ) and viscosity (μ) are averaged locally from the two phases, weighted with the local ϕ:

$$\begin{cases} \rho(\mathbf{X}) = \phi(\mathbf{X})\,\rho_g + (1-\phi(\mathbf{X}))\,\rho_l, \\ \mu(\mathbf{X}) = \phi(\mathbf{X})\,\mu_g + (1-\phi(\mathbf{X}))\,\mu_l. \end{cases} \tag{21}$$

The surface tension force is defined according to the Continuum Surface Force (CSF) model (Brackbill et al., 1992), where k indicates the local curvature, $\mathbf{n}$ the normal vector and δ the interface thickness, which is approximated as $\delta \approx |\nabla(\phi)|$:

$$\mathbf{f}_\sigma = \sigma\,k\,\mathbf{n}\,\delta \approx \sigma\,k\,\nabla\phi \tag{22}$$

Eq. (20) are solved adopting a fractional step method, advanced in time with a second-order Adam-Bashfort scheme and using a Fast Poisson Solver to enforce the zero divergence of the velocity field.

3.3. Computational setup

A cylindrical geometry is considered to model the vertical pipe, with the diameter set according to the prescribed value of χ. Belleri, 2025 established the domain size and grid resolution required to guarantee mesh-independent results for the unconfined case. He determined a domain size of $12d_{eq}$ in the gravity direction; together with a uniform grid resolution: $\Delta x = \Delta y = \Delta z = d_{eq}/30$. Following these results, the same domain length and grid resolution are adopted in the present work, with no-slip boundary conditions imposed at the pipe wall and periodic boundary conditions applied along the unconfined axis. Furthermore, he showed that bubble shape and terminal velocity do not depend on viscosity ratio (μ_r) and density ratio (ρ_r), which are therefore a priori set to 10^{-2}. The gravitational acceleration, the bubble initial diameter and the continuum phase density are kept constant among all cases ($g = 9.8m/s^2$, $d_{eq} = 0.01216m$, $\rho_l = 875kg/m^3$); while the liquid phase viscosity (μ_l) and the surface tension (σ) are determined from Eötvös and Morton numbers.

4. Results

Globally, 93 combinations of Eo and Mo were considered, selected as a subset of the simulations performed by Belleri, 2025. These combinations span the ranges $10^{-11} \le Mo \le 10^8$ and $10^{-2} \le Eo \le 10^3$, ensuring coverage of all bubble shape regimes. Each case was simulated for four confinement levels: $\chi = 0.167$, 0.25, 0.5 and 0.667; corresponding to pipe to bubble equivalent diameter ratios ($1/\chi$) of 6, 4, 2 and 1.5, respectively. The results in terms of Re, E and BDF of the 372 simulations are reported in the table in appendix A. Additionally, the results for the unconfined case, derived from the simulations performed by Belleri, 2025, are reported in appendix B. For wobbling bubbles, which exhibit time-dependent shape oscillations, average values of E and BDF are reported and marked with *, whereas bubbles undergoing breakup are marked with −. Bubbles in different regimes are shown for all the confinement levels in Fig. 4.

4.1. Terminal velocity

The influence of confinement on bubble terminal velocity is visualized using Grace plots (Fig. 5), colored according to the percentage variation in U with respect to the corresponding unconfined value, taken from Tomiyama et al., 1998. Consistent with previous studies, it clearly emerges that the terminal velocity decreases as the confinement becomes tighter. However, this reduction is not uniform across the entire parameter space: it is significantly more pronounced at lower Eötvös numbers and higher Morton numbers, implying that confinement is intrinsically coupled with the governing dimensionless groups and cannot be treated as an independent effect. Classical correlations from the literature failed to include such dependence, resulting in models with a limited range of applicability. In light of the above, a general correlation for the velocity retardation is formulated, valid over a wide range of Eo and Mo and expressed as a function of χ, Eo, Mo:

$$\frac{U}{U_{\chi=0}} = \frac{1}{1 + 32.6\left(\frac{Mo}{Eo^6}\right)^{0.067}\chi^{2.3}} \tag{23}$$

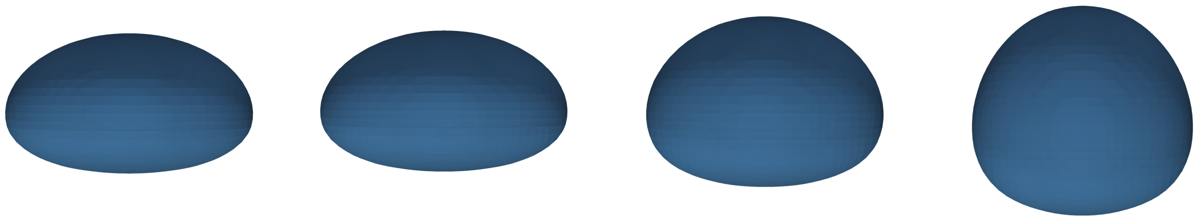

(a) Ellipsoidal bubble, $\log_{10}Mo = -3,\ Eo = 10$

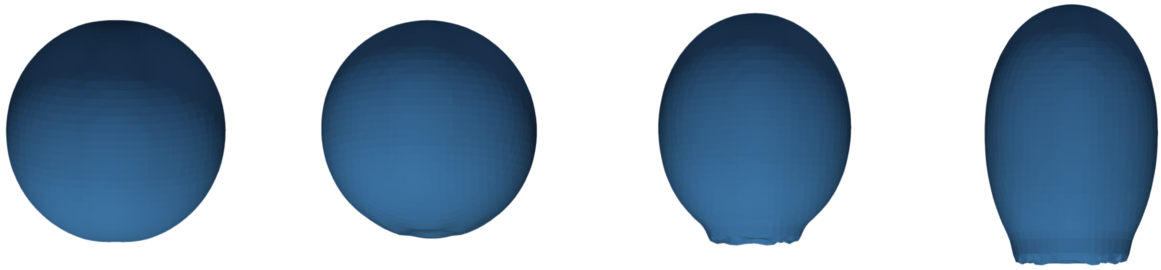

(b) Spherical bubble, $\log_{10}Mo = 7,\ Eo = 300$

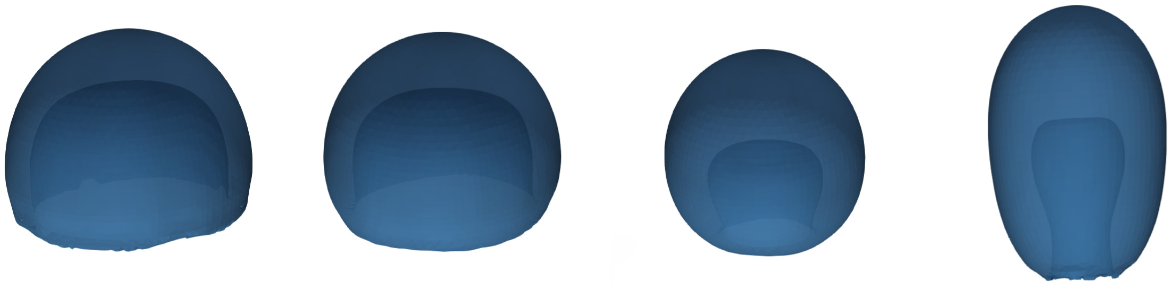

(c) Skirted bubble, $\log_{10}Mo = 2,\ Eo = 300$

Figure 4: Bubble regimes observed under different confinement conditions. Columns from left to right correspond to $\chi = 0.667,\ 0.5,\ 0.25$ and 0.167

The proposed formulation is restricted to particle-like bubble dynamics, identified according to Eq. (14). In fact, for confinement levels exceeding the onset of Taylor-like behavior, U becomes independent of χ, thus requiring a structurally different model, whose development demands a robust and dedicated dataset.
Parity plots are used to compare the proposed correlation with simulation results (Fig. 6b) and with available literature models (Fig. 6a). Good agreement with DNS data is observed across the entire parameter space, confirming the overall predictive consistency of the model. Conversely, comparison with literature models shows that Eq. (23) applies a weaker correction, resulting in systematically higher predicted values of U, particularly in the low-velocity regime.
The confinement effect predicted by Eq. (23) is illustrated in Fig. 7, where the velocity retardation is shown as a function of χ for selected values of Eo and Mo. The correlation recovers the unconfined limit as $\chi \to 0$ and predicts a progressively stronger reduction in terminal velocity as confinement increases, which is more pronounced at lower Eo and higher Mo.

While the proposed correlation enables predicting confinement-induced velocity reduction, a deeper physical interpretation can be obtained by examining the power balance governing the bubble motion.
In steady conditions, the power associated with buoyancy (P_B) must balance the power dissipated by drag (P_D):

$$P_B = P_D \tag{24}$$

The buoyancy power can be expressed in terms of the buoyancy force F_B as:

$$P_B = F_B\,U = (\Delta\rho\, g\, V_g)\,U \tag{25}$$

where V_g denotes the bubble volume.

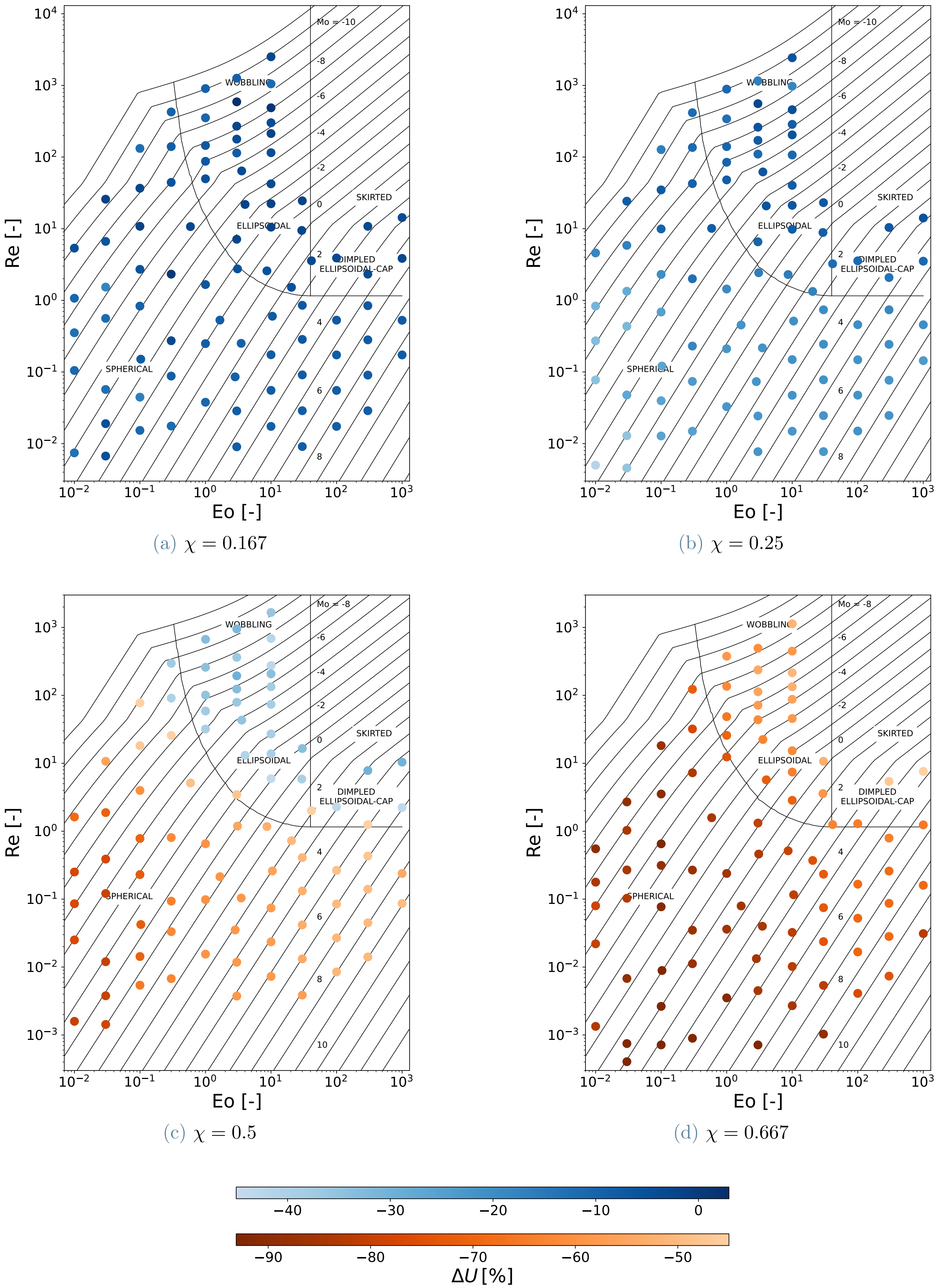

(a) $\chi = 0.167$

(b) $\chi = 0.25$

(c) $\chi = 0.5$

(d) $\chi = 0.667$

Figure 5: Simulation data plotted in the Grace diagram, colored according to the percentage variation of the terminal velocity relative to the unconfined case. A common color bar is used.

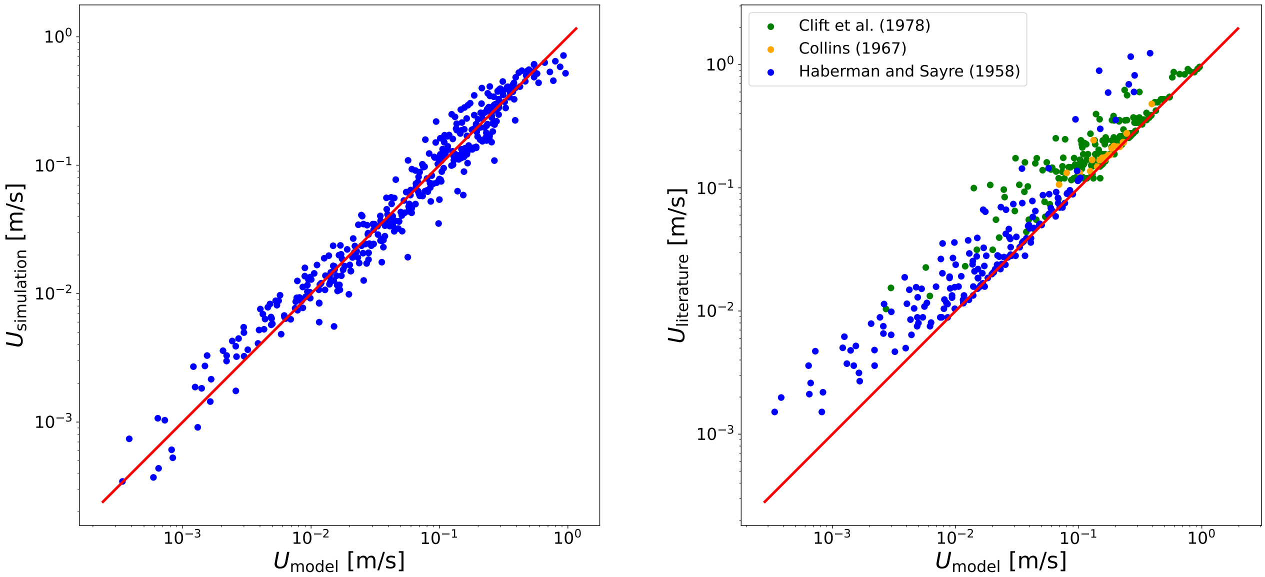

(a) Comparison with simulation data.

(b) Comparison with literature models (Eq. (11) to (13)).

Figure 6: Parity plots comparing bubble terminal velocity predictions from Eq. (23) with simulation and literature data. The bisector indicates perfect agreement.

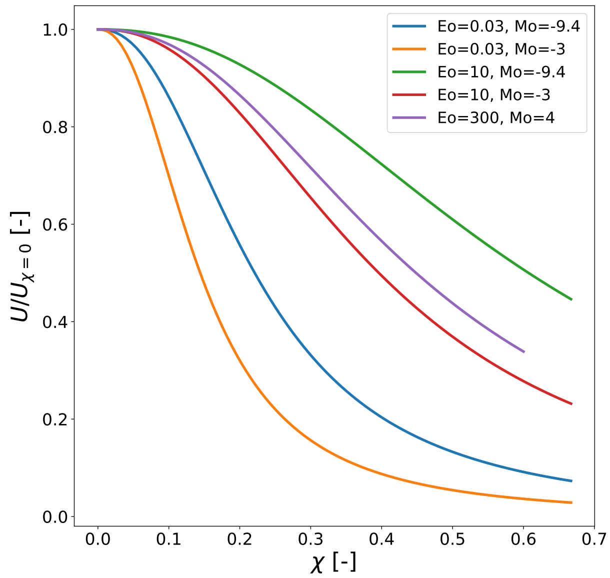

Figure 7: Velocity retardation $U/U_{\chi=0}$ as predicted by Eq. (23), plotted as a function of the confinement ratio χ for various combinations of Eötvös and Morton numbers. Curves are truncated at the onset of Taylor-like behavior, identified according to Eq. (14). Legend values of Mo are given in base-10 logarithmic form.

Since $\mu_g << \mu_l$, the viscous dissipation mainly occurs in the liquid (Harper, 1972) and, according to Batchelor, 1967, can be expressed as:

$$P_D = -\int_{V_l} 2\mu\, \mathbf{S} : \mathbf{S}\, dV \tag{26}$$

where $\mathbf{S} = 1/2\left(\nabla\mathbf{u} + \nabla\mathbf{u}^T\right)$ denotes the strain rate tensor and V_l the liquid domain.
For fixed fluid properties and bubble volume, F_B is independent of χ; consequently, variations in P_D directly translate into changes in U. In light of the above, it is possible to justify any variation in terminal velocity just analyzing viscous dissipation.

In the subsequent analysis, only bubbles having $Re << 1$ and undergoing negligible deformation over the entire range of confinement levels are considered; thereby isolating the effects of confinement on the velocity field from those associated with deformation. In Fig. 8 the total viscous dissipation computed for all values of χ is reported. A systematic decrease is observed as χ increases, further indicating a wall-induced terminal velocity reduction.
However, confinement not only affects the global value of P_D, but also, crucially, its local distribution within the liquid domain. To quantify this effect, the liquid volume is partitioned into three regions, namely the bubble-wall gap, the front region upstream of the bubble and the rear region downstream of it. The fraction of P_D generated in each region is computed for all χ and reported in Fig. 9a. For weak confinements, significant contributions arise from the front and rear regions, indicating that P_D is strongly associated with the displacement of liquid upstream of the bubble and the replenishment of the volume downstream of it. As confinement becomes stronger, the main source of dissipation shifts towards the gap region, reaching 80% for $\chi = 0.667$. In fact, the liquid is forced to flow through a narrower passage, resulting in higher local velocities, and the no-slip condition at the wall must be satisfied over a much shorter distance, leading to stronger local velocity gradients.
To further investigate this effect, $\mathbf{S}$ is decomposed in its contributions:

$$\begin{gathered} S_x = \frac{\partial u_x}{\partial x}, \qquad S_y = \frac{\partial u_y}{\partial y}, \qquad S_z = \frac{\partial u_z}{\partial z}, \\ S_{xy} = \frac{1}{2}\left(\frac{\partial u_x}{\partial y} + \frac{\partial u_y}{\partial x}\right), \qquad S_{zy} = \frac{1}{2}\left(\frac{\partial u_z}{\partial y} + \frac{\partial u_y}{\partial z}\right), \qquad S_{xz} = \frac{1}{2}\left(\frac{\partial u_x}{\partial z} + \frac{\partial u_z}{\partial x}\right). \end{gathered} \tag{27}$$

with $S_x \simeq S_z$ and $S_{xy} \simeq S_{zy}$ thanks to the axisymmetric nature of the problem. The relative weight of each contribution is computed and reported in Fig. 9b. S_{xy} exhibits an increase with χ, indicating that viscous dissipation becomes dominated by transverse velocity gradients, consistent with the liquid transitioning from higher velocities in the gap to zero velocity at the wall over a shorter distance. Conversely, a decrease in S_y is observed, further suggesting that dissipation associated with streamwise velocity gradients, which govern upstream liquid displacement and downstream replenishment, becomes relatively less significant.
Importantly, the relative percentage contributions remain essentially unchanged across different Eo–Mo combinations (not shown), indicating that the redistribution of viscous dissipation is primarily driven by confinement rather than by fluid properties. Similar conclusions have been reported by Dabiri and Bhuvankar, 2016, who provided visualizations of the viscous dissipation in the liquid domain, highlighting its concentration within the bubble–wall gap.

This redistribution of P_D suggests that confinement primarily enhances viscous dissipation within the bubble-wall gap. Consequently, if the bubble terminal velocity was assumed to remain unchanged across all the confinement levels, P_D would be expected to increase with χ. Conversely, recalling Eq. (25), P_B would remain unchanged under the same assumption.

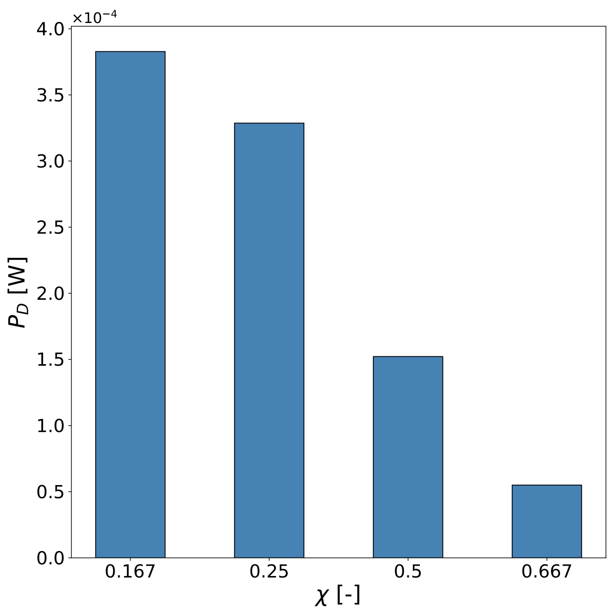

Figure 8: Total viscous dissipation reported for all considered values of χ. Results refer to a system with $Eo = 1.661$ and $\log_{10}Mo = -1.32$.

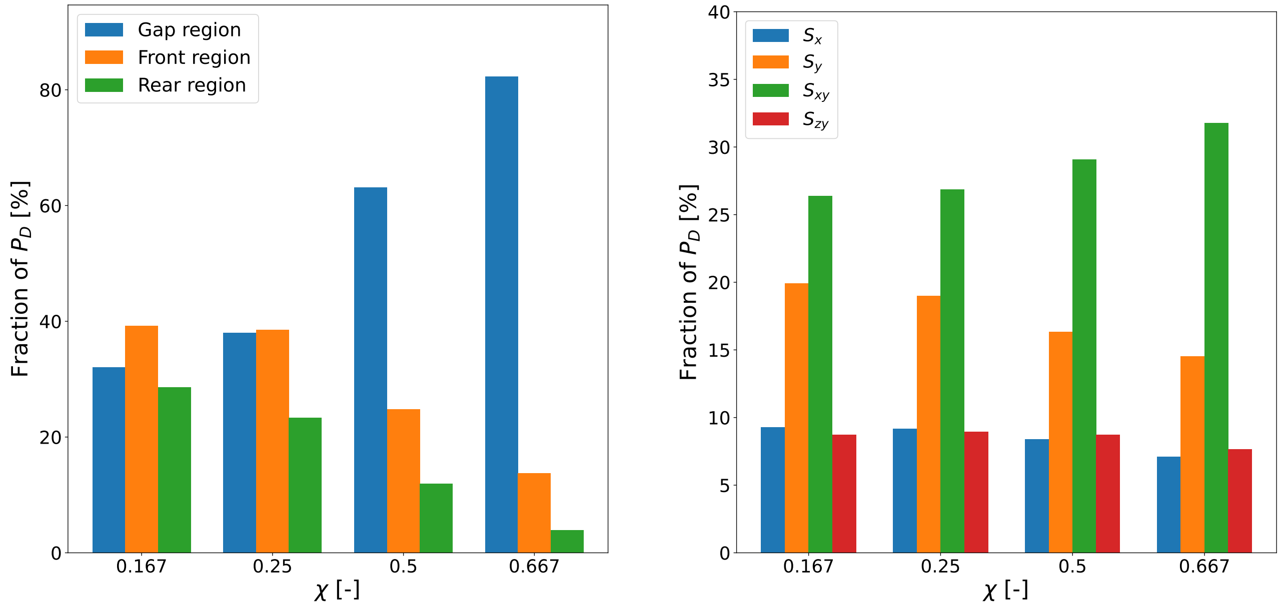

(a) Percentage contribution to the total viscous dissipation of the bubble–wall gap region, front region and rear region.

(b) Percentage contribution to the total viscous dissipation of the different velocity-gradient components: S_x, S_y, S_{xy} and S_{zy} as defined in Eq. (27).

Figure 9: Percentage contributions to the total viscous dissipation for all considered values of χ. Results refer to a system with $Eo = 1.661$ and $\log_{10}Mo = -1.32$.

As a result, the power balance in Eq. (24) would no longer be satisfied, implying that the bubble terminal velocity must adjust in response to confinement variations.
To quantify this adjustment, the scaling of P_B and P_D with respect to U is examined for a fixed geometry. From Eq. (25), P_B is linear in U.
Under the hypothesis $Re << 1$, inertial effects are negligible and therefore the non-linear convective term in Eq. (20) can be neglected. Moreover, the gravitational body-force term and the surface tension term, expressed in gradient form according to Eq. (22), can be included in a modified pressure, defined as: $p' = p - \rho \mathbf{g} \cdot \mathbf{x} - \sigma k \phi$. Under steady-state conditions, the governing equations reduce to the Stokes system (Stokes, 1851):

$$\begin{cases} -\nabla p' + \nabla \cdot \left[\mu (\nabla \mathbf{u} + \nabla \mathbf{u}^T) \right] = 0 \\ \nabla \cdot \mathbf{u} = 0 \end{cases} \tag{28}$$

Eq. (28) is linear in $\mathbf{u}$, therefore the spatial structure of the velocity field is uniquely determined and a change in U simply rescales the entire field, as shown by the classical solution by Hadamard, 1911 and Rybczynski, 1911. It follows that the local liquid velocity $\mathbf{u}_l$ scales linearly with U and therefore, recalling Eq. (26), P_D scales quadratically with U.
Combining these scalings and recalling that confinement does not directly affect P_B (which depends on χ only through the resulting value of U), whereas it enhances P_D:

$$P_B \sim U, \qquad P_D \sim C(\chi)\, U^2 \tag{29}$$

where $C(\chi)$ is a coefficient accounting for the effect of χ on viscous dissipation.
Since $C(\chi)$ increases with the confinement, the intersection $P_B = P_D$ is shifted towards lower values of both power and U. In light of the above, under the hypothesis of a fixed bubble shape and $Re << 1$, bubble terminal velocity must decrease as confinement is increased. This theoretical prediction is fully consistent with simulation results, which show a systematic reduction of the viscous dissipation (Fig. 8) and of the bubble terminal velocity with increasing confinement (Fig. 5).

4.2. Aspect ratio

As introduced by several literature works, confinement induces a progressive elongation of the bubble in the flow direction, a trend that can be qualitatively appreciated in Fig. 4. This behavior can be explained in terms of viscous dissipation, which was shown to increase significantly in the bubble–wall gap region with increasing confinement.

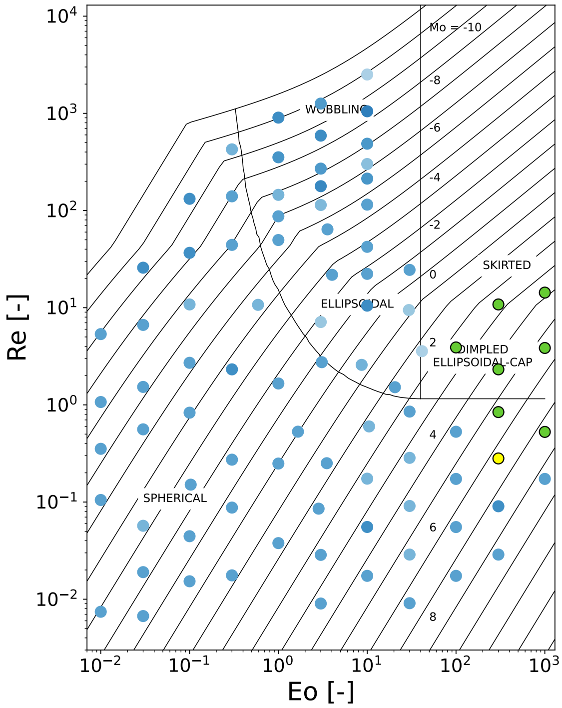

(a) $\chi = 0.167$

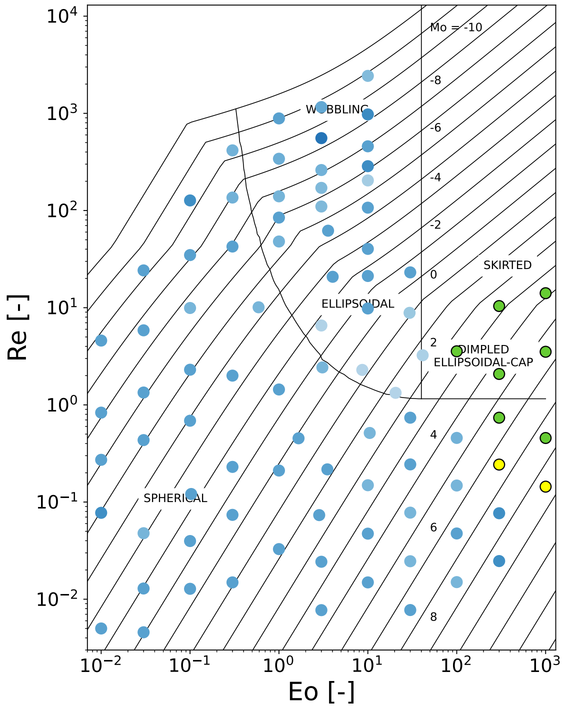

(b) $\chi = 0.25$

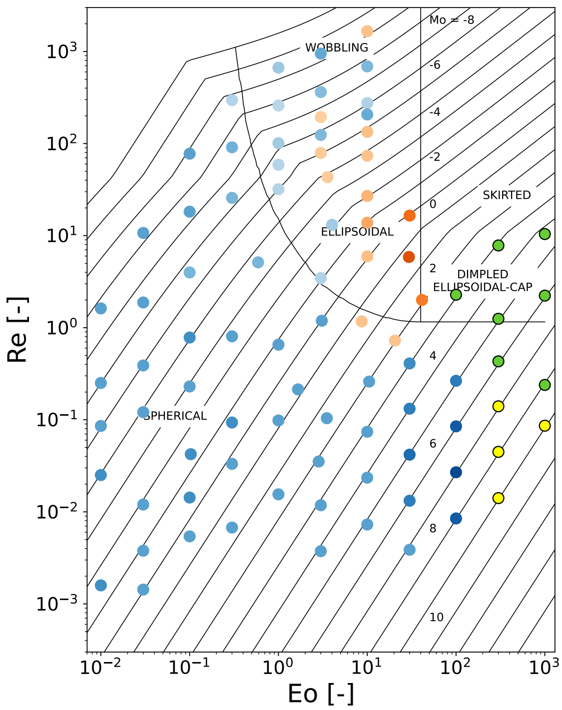

(c) $\chi = 0.5$

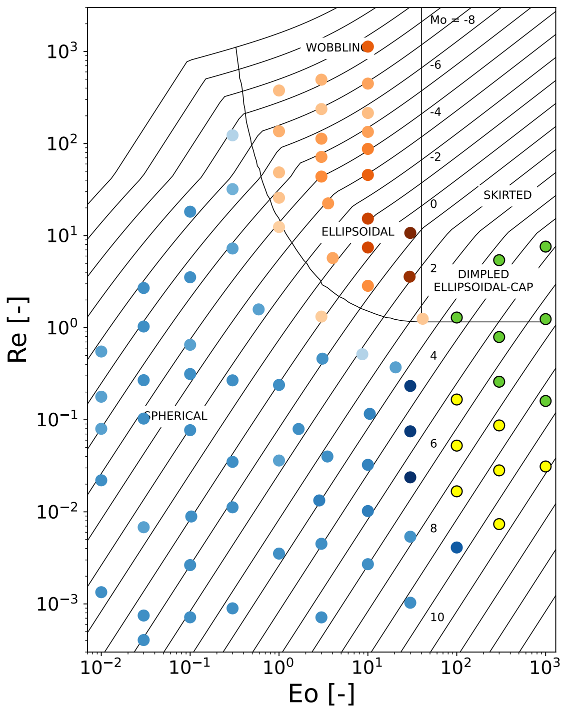

(d) $\chi = 0.667$

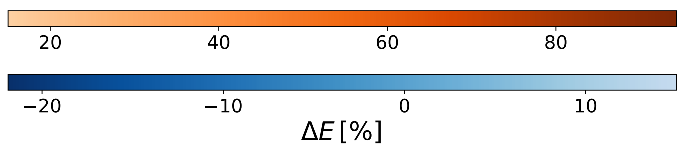

Figure 10: Simulation data plotted in the Grace diagram, colored according to the percentage variation of the aspect ratio with respect to the unconfined case. A common color bar is used.

This implies that deformation involving lateral expansion of the interface requires overcoming increasingly large viscous stresses within the gap region. As a result, lateral deformation becomes progressively penalized compared to deformation along the rise direction, leading to more longitudinally elongated bubble shapes.
This change of shape is reflected by a variation of the bubble aspect ratio, as shown in Fig. 10, where simulation data are represented on Grace plots and colored according to the percentage variation of E with respect to the unbounded case. Skirted bubbles are represented separately, with yellow and green dots, since E is not a meaningful metric to describe their shape. In particular, green dots indicate bubbles that already exhibit a skirt or a dimple in unconfined conditions, whereas yellow dots indicate bubbles that are initially spherical. A higher density of yellow dots is observed for tighter confinements, suggesting that wall effects promote the development of dimpled ellipsoidal-cap and skirted configurations, consistent with Bhaga (1977). An example of this behavior can be observed in Fig. 4b.
$\Delta E_{\%}$ is found to be minimal for $\chi = 0.167$ and $\chi = 0.25$, suggesting that confinement ratios below $\chi \simeq 0.25$ do not significantly affect the bubble shape. Similarly to the terminal velocity, the variation of E is not uniform across the entire range of governing non-dimensional parameters. Bubbles belonging to the ellipsoidal regime exhibit an increase in aspect ratio as confinement becomes stronger. In fact, wall effect suppresses lateral deformation and enhances axial elongation, thereby reducing the disparity between the two dimensions characterizing unbounded conditions. This results in a bubble shape closer to sphericity, as emerges from Fig. 4a, where an originally ellipsoidal bubble evolves towards a less deformed shape under confinement. Since the two principal axes become more similar, an increase of E is observed.
For bubbles belonging to the spherical regime, the tendency to deform depends on the Eötvös number. For $Eo \lesssim 20$, surface tension forces dominate the dynamics, effectively counteracting any deformation tendency. Therefore, wall-induced axial elongation remains limited and bubbles in this regime maintain nearly spherical shapes, with $E \simeq 1$. Instead, for $Eo \gtrsim 20$, surface tension forces become relatively weaker and are no longer able to counteract wall-induced deformation tendency. As a consequence, axial elongation is enhanced, resulting in an appreciable decrease in E.

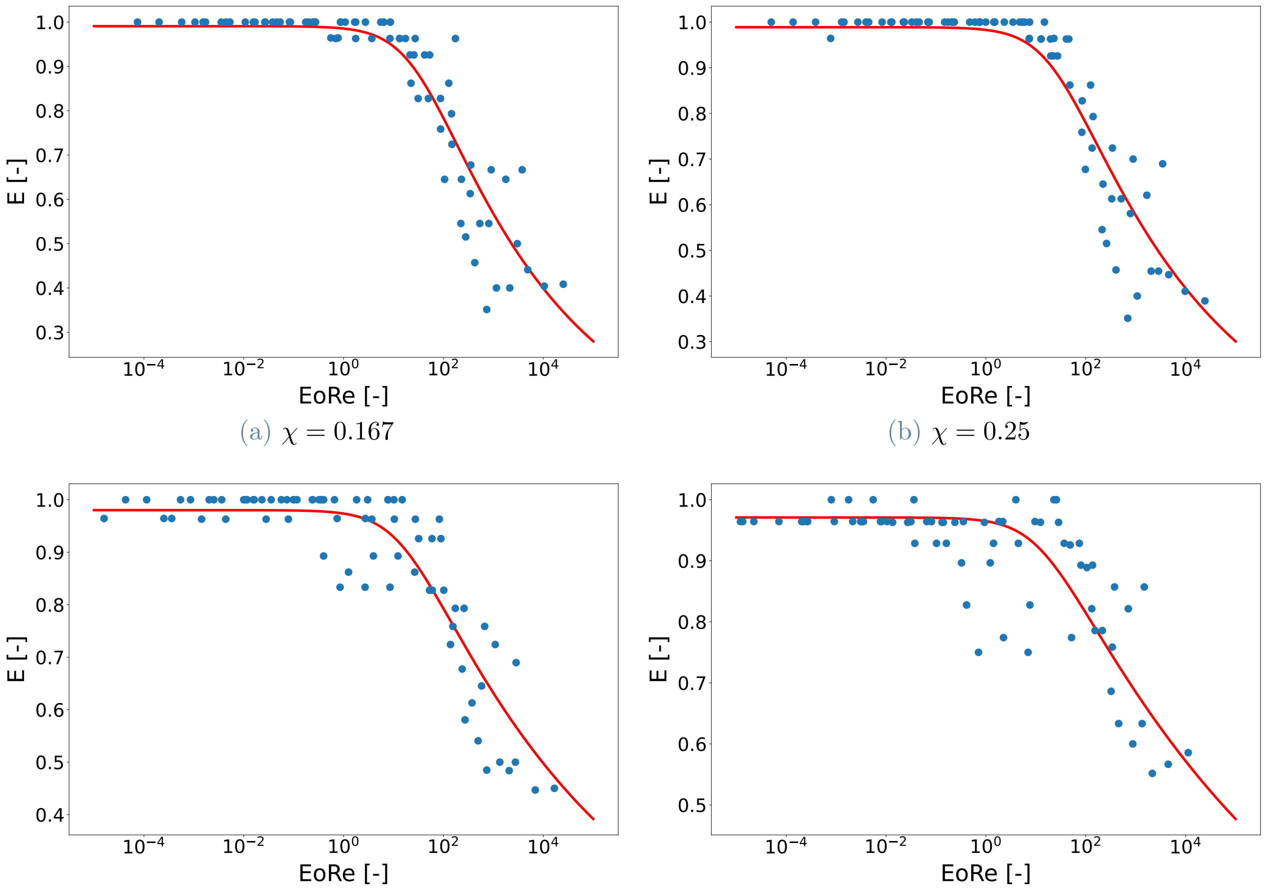

(a) $\chi = 0.167$ (b) $\chi = 0.25$ (c) $\chi = 0.5$ (d) $\chi = 0.667$

Figure 11: Predicted E as a function of $EoRe$, obtained from the proposed correlation (Eq. (30)) and compared with the corresponding simulation data. Each panel corresponds to a different confinement ratio.

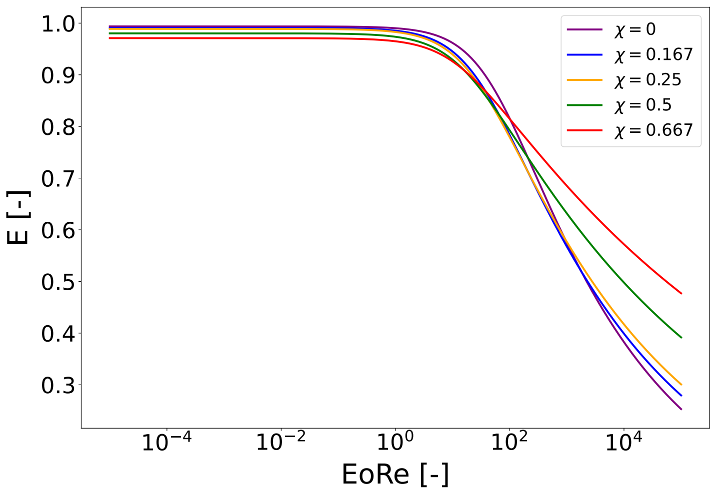

Figure 12: Predicted E as a function of $EoRe$, obtained from the proposed correlation (Eq. (30)), comparing trends across different confinement ratios.

Once again, since the dependence of E on wall effects varies across the parameter space, a correction proportional only to χ is not accurate. Instead, a new expression for E is proposed, starting from Eq. (9) and directly incorporating χ as an additional governing parameter:

$$E = \frac{1 - 0.04\,\chi}{(1 + (0.02 + 0.1\,\chi)\,EoRe)^{0.18 - 0.15\,\chi}} \tag{30}$$

The proposed correlation naturally recovers Eq. (9) for $\chi \to 0$.
Eq. (30) is plotted as a function of $EoRe$ in Fig. 11, together with the corresponding simulation data, while Fig. 12 compares the predicted curves for all confinement ratios.

4.3. Bubble deformation factor

Changes in bubble shape directly translate into variations of the interfacial area and therefore of the bubble deformation factor. As previously introduced, the BDF is inversely related to the aspect ratio for convex bubble shapes; therefore, in such case its trend can be directly inferred from that of E. As discussed above, ellipsoidal bubbles progressively approach a more spherical shape under confinement, with E increasing with χ, implying a decrease in BDF. Conversely, spherical bubbles at $Eo \gtrsim 20$ undergo axial elongation, leading to a reduction in E and, consequently, to a slight increase in BDF. Similarly to E, the BDF remains almost unchanged for $\chi \leq 0.25$, while appreciable variations are observed for $\chi = 0.5$ and 0.667.
The BDF becomes particularly relevant for skirted and dimpled bubbles, being the only metric capable of quantifying their deformation. Wall effect promotes the onset of a skirt for bubbles at high Eo by enhancing deformation at the bubble base and favoring interface stretching towards the rear. This leads to the formation of an inner surface and, consequently, to an increase of interfacial area. Such physical mechanism combines with the vertical elongation discussed in the previous section, with both effects contributing to the overall bubble interfacial surface.
For bubbles at low Re, which would be spherical or dimpled ellipsoidal under unconfined conditions, skirt formation and axial elongation act in the same direction, resulting in a net increase in BDF. This can be qualitatively observed in Fig. 4b, where an originally spherical bubble develops a rear concavity and undergoes vertical elongation under confinement.
Conversely, at higher Re, bubbles are already skirted under unconfined conditions, exhibiting a widely open skirt characterized by a large inner area and, consequently, high BDF. As confinement increases, the lateral opening progressively decreases, leading to a significant reduction of the inner surface (Fig. 4c). This effect outweighs the wall-induced axial elongation, resulting in an overall reduction of the BDF.
Analogously to E, a new correlation for BDF is proposed in terms of for the relevant non-dimensional groups and χ. In particular, as shown by Belleri, 2025, BDF is found to be function of We^2/Eo:

$$BDF = 1 + (0.025 + 4.49\,\chi^{6.5})\,We^2/Eo \tag{31}$$

Eq. (31) is plotted as a function of We^2/Eo in Fig. 13 for all confinement levels, together with the corresponding simulation data, while Fig. 14 compares the predicted curves for all confinement ratios.

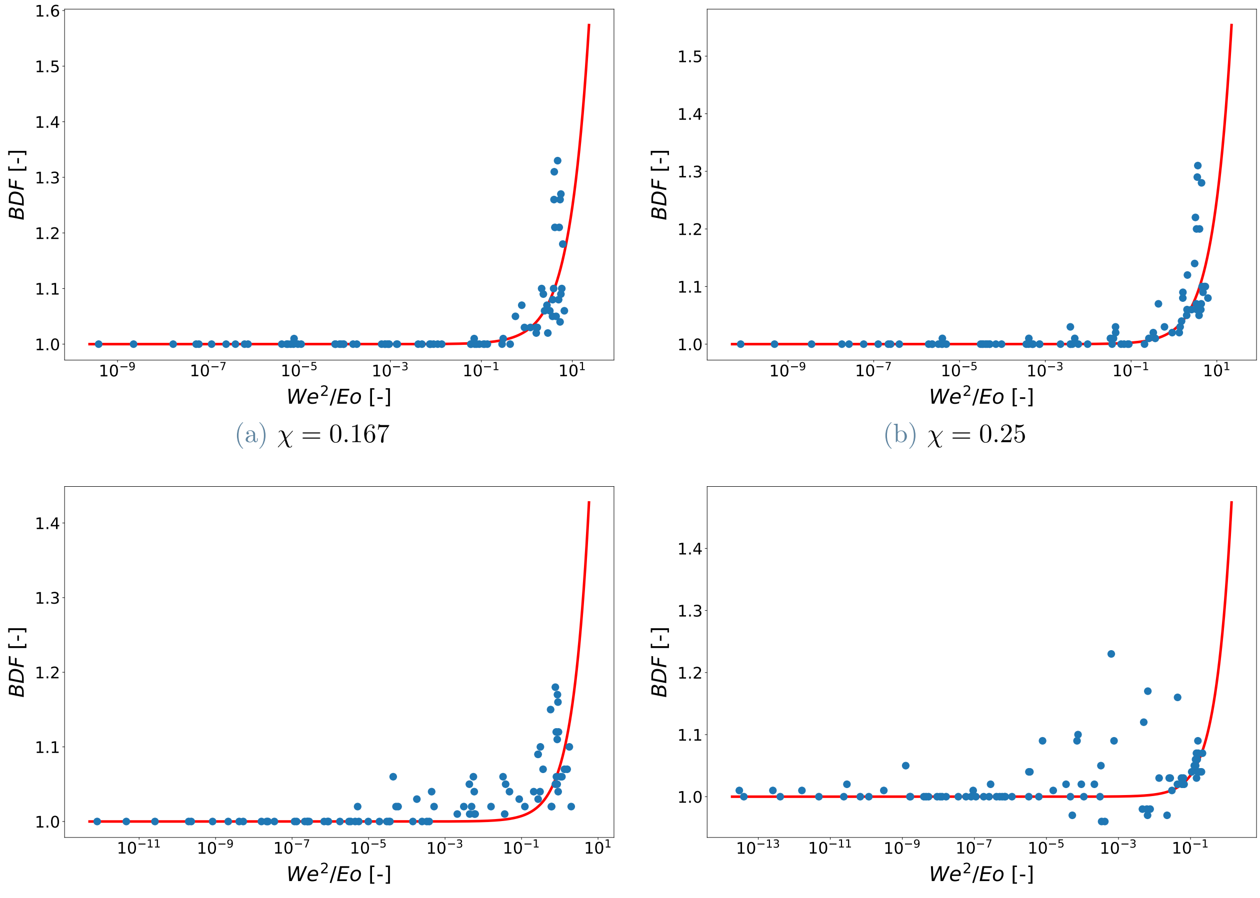

(a) $\chi = 0.167$

(b) $\chi = 0.25$

(c) $\chi = 0.5$

(d) $\chi = 0.667$

Figure 13: Predicted BDF as a function of We^2/Eo, obtained from the proposed correlation (Eq. (31)) and compared with the corresponding simulation data. Each panel corresponds to a different confinement ratio.

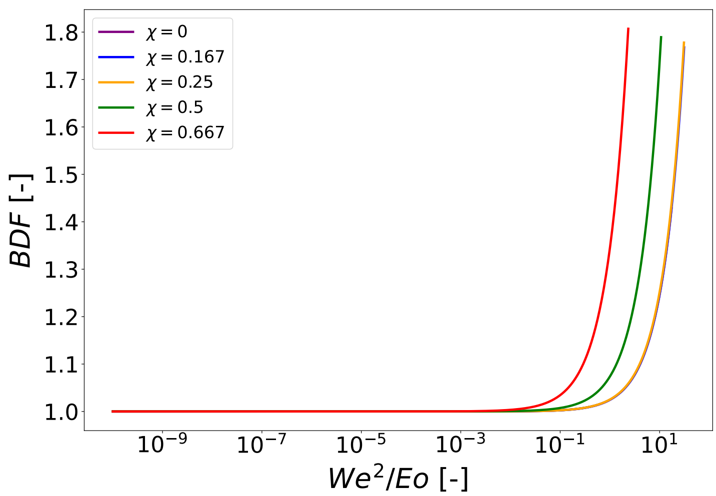

Figure 14: Predicted BDF as a function of We^2/Eo, obtained from the proposed correlation (Eq. (31)), comparing trends across different confinement ratios.

5. Conclusions

The dynamics and deformation of a single gas bubble rising in a vertical pipe have been investigated by means of VOF-based DNS code. Previous analyses performed under unbounded conditions have been extended to confined geometries, investigating wall effects over a wide range of Eötvös and Morton through systematic variations of the confinement ratio.

Simulations results show that confinement has a strong impact on bubble terminal velocity, shape and interfacial area. In particular, consistent with literature results, a wall-induced reduction of the terminal velocity was observed, with a magnitude that varies with fluid properties. A correlation for the velocity retardation was formulated (Eq. (23)), expressed in terms of Eo, Mo and χ, and valid over a wide range of fluid properties, provided that particle-like behavior is preserved. The proposed model was shown to slightly overestimate available literature data.

It was shown that confinement promotes longitudinal elongation and an earlier onset of skirted and dimpled configurations, with fluid properties governing these effects and resulting in non-uniform trends across the Eo-Mo space. Subsequently, new correlations for aspect ratio (Eq. (30)) and bubble deformation factor (Eq. (31)) were formulated, explicitly incorporating the confinement ratio and the relevant non-dimensional groups, namely $EoRe$ for E and We^2/Eo for BDF. These correlations address the lack of predictive models available in the literature for bubble shape and interfacial area under confined conditions.

A physical interpretation of the wall-induced velocity reduction was obtained by analyzing the effect of confinement on viscous dissipation, showing that it becomes increasingly concentrated within the bubble–wall gap, thereby modifying the power balance and leading to a lower equilibrium velocity.

Overall, the proposed predictive models provide a unified description for single-bubble terminal velocity, aspect ratio and bubble deformation factor over a wide range of fluid properties and confinement levels; thereby improving the modeling of bubbly flows in confined conditions.

Future work should extend the analysis to higher confinement ratios, where bubbles exhibit Taylor-like behavior requiring structurally different modeling approaches, and account for surfactant effects, which significantly alter interfacial dynamics. The present framework could also be extended to different reactor geometries, such as rectangular or annular channels, and to varying liquid flow conditions, including co-current and counter-current regimes. As a next step, the transition to multi-bubble systems should be investigated to move towards more realistic operating conditions. In particular, bubble–bubble interactions, coalescence and breakup phenomena should be systematically analyzed, since they directly influence interfacial area and gas holdup and therefore mass and energy transfers among phases.

References

A. Acrivos and T.D. Taylor. Heat and mass transfer from single spheres in stokes flow. *Physics of Fluids*, 5: 387–394, 1962.

S. Aoyama, K. Hayashi, S. Hosokawa, and A. Tomiyama. Shapes of ellipsoidal bubbles in infinite stagnant liquids. *International Journal of Multiphase Flow*, 79:23–30, 2016. doi: 10.1016/j.ijmultiphaseflow.2015.10.009.

G.K. Batchelor. *An Introduction to Fluid Dynamics.* Cambridge University Press, Cambridge, England, 1967.

R. Belleri. Direct numerical simulation of a single rising bubble: Determining aspect ratio and interfacial area. Master's thesis, Politecnico di Milano, 2025.

G. Besagni and N.G. Deen. Aspect ratio of bubbles in different liquid media: A novel correlation. *Chemical Engineering Science*, 215:115383, 2020. doi: 10.1016/j.ces.2019.115383.

G. Besagni and F. Inzoli. Bubble size distributions and shapes in annular gap bubble column. *Experimental Thermal and Fluid Science*, 74:27–48, 2016. doi: 10.1016/j.expthermflusci.2015.12.002.

G. Besagni, F. Inzoli, and T. Ziegenhein. Two-phase bubble columns: A comprehensive review. *ChemEngineering*, 2:13, 03 2018. doi: 10.3390/chemengineering2020013.

D. Bhaga. *Bubbles in viscous liquids: Shapes, wakes and velocities.* Phd thesis, McGill University, Montreal, Canada, 1977.

J.U. Brackbill, D.B. Kothe, and C. Zemach. A continuum method for modeling surface tension. *Journal of Computational Physics*, 100(2):335–354, 1992.

I. Cannon, G. Soligo, and M.E. Rosti. Morphology of clean and surfactant-laden droplets in homogeneous isotropic turbulence. *Journal of Fluid Mechanics*, 987:A31, 2024. doi: 10.1017/jfm.2024.314.

R. Clift, J.R. Grace, and M.E. Weber. *Bubbles, Drops, and Particles.* Academic Press, 1978.

R. Collins. The influence of confinement on the motion of large gas bubbles in liquids. *Journal of Fluid Mechanics*, 28:97–118, 1967.

M. Coutanceau and A. Texier. Experimental investigation of the creeping motion of a drop in a vertical tube. *Experiments in Fluids*, 4(5):241–246, 1986. doi: 10.1007/BF00369115.

S. Dabiri and P. Bhuvankar. Scaling law for bubbles rising near vertical walls. *Physics of Fluids*, 28(6):062101, 06 2016. ISSN 1070-6631. doi: 10.1063/1.4948464.

R.M. Davies and G. Taylor. The Mechanics of Large Bubbles Rising through Extended Liquids and through Liquids in Tubes. *Proceedings of the Royal Society of London Series A*, 200(1062):375–390, February 1950. doi: 10.1098/rspa.1950.0023.

A. Esmaeeli and G. Tryggvason. Direct numerical simulations of bubbly flows. part 1. low reynolds number arrays. *Journal of Fluid Mechanics*, 377:313–345, 1998. doi: 10.1017/S0022112098002850.

L.S. Fan and K. Tsuchiya. *Bubble Wake Dynamics in Liquids and Liquid-Solid Suspensions.* Butterworth-Heinemann, Oxford, 1990.

J.R. Grace. Shapes and velocities of bubbles rising in infinite liquids. *Transactions of the Institution of Chemical Engineers*, 51:116–120, 1973.

W.L. Haberman and R.M. Sayre. Motion of rigid and fluid spheres in stationary and moving liquids. Technical Report Report 1143, David Taylor Model Basin, 1958.

J.S. Hadamard. Mouvement permanent lent d'une sphère liquide et visqueuse dans un liquide visqueux. *Comptes Rendus de l'Académie des Sciences*, 152:1735–1737, 1911.

J.F. Harper. The motion of bubbles and drops through liquids. volume 12 of *Advances in Applied Mechanics*, pages 59–129. Elsevier, 1972. doi: https://doi.org/10.1016/S0065-2156(08)70133-9.

K. Hayashi and A. Tomiyama. A drag correlation of fluid particles rising through stagnant liquids in vertical pipes at intermediate reynolds numbers. *Chemical Engineering Science*, 64:3019–3028, 2009.

K. Hayashi, R. Kurimoto, and A. Tomiyama. Dimensional analysis of terminal velocity of a taylor bubble in a vertical pipe. *Multiphase Science and Technology*, 22:197–210, 01 2010. doi: 10.1615/MultScienTechn.v22.i3.20.

C.W. Hirt and B.D. Nichols. Volume of fluid (vof) method for the dynamics of free boundaries. *Journal of Computational Physics*, 39(1):201–225, 1981.

S. Ii, K. Sugiyama, S. Takeuchi, S. Takagi, Y. Matsumoto, and F. Xiao. An interface capturing method with a continuous function: the THINC method with multi-dimensional reconstruction. *Journal of Computational Physics*, 231(5):2328–2358, 2012.

M. Ishii and T.C. Chawla. Local drag laws in dispersed two-phase flow. Technical Report ANL-79-105 / NUREG/CR-1230, Argonne National Laboratory, 1979.

R. Kurimoto, K. Hayashi, and A. Tomiyama. Terminal velocities of clean and fully-contaminated drops in vertical pipes. *International Journal of Multiphase Flow*, 49:8–23, 2013. ISSN 0301-9322. doi: https://doi.org/10.1016/j.ijmultiphaseflow.2012.08.001.

D. Legendre and R. Zenit. Gas bubble dynamics. *Review of Modern Physics*, 97, 2025.

D. Legendre, R. Zenit, and J. R. Velez-Cordero. On the deformation of gas bubbles in liquids. *Physics of Fluids*, 24(4):043303, 2012. doi: 10.1063/1.4705527.

V.G. Levich. *Physicochemical Hydrodynamics.* Prentice-Hall, Englewood Cliffs, NJ, 1962.

A.C. Lochiel and P.H. Calderbank. Mass transfer in the continuous phase around axisymmetric bodies of revolution. *Chemical Engineering Science*, 19(7):471–484, 1964.

S. Maalej, B. Benadda, and M. Otterbein. Interfacial area and volumetric mass transfer coefficient in a bubble reactor at elevated pressures. *Chemical Engineering Science*, 58:2365–2376, 2003. doi: 10.1016/S0009-2509(03)00064-7.

Z. Mei and X. Cheng. Modeling of interfacial area for single deformed bubble based on vof method. *Nuclear Engineering and Design*, 395:111864, 2022. doi: 10.1016/j.nucengdes.2022.111864.

Z. Mei and X. Cheng. Analysis of single bubble dynamics based on vof method. *Annals of Nuclear Energy*, 208:110757, 2024. doi: 10.1016/j.anucene.2024.110757.

S. Mirjalili, S.S. Jain, and M.S. Dodd. Interface-capturing methods for two-phase flows: An overview and recent developments. *Center for Turbulence Research - Annual research brief*, pages 117–135, 2017.

D.W. Moore. The boundary layer on a spherical gas bubble. *Journal of Fluid Mechanics*, 16:161–176, 1963.

D.W. Moore. The velocity of rise of distorted gas bubbles in a liquid of small viscosity. *Journal of Fluid Mechanics*, 23:749–766, 1965. doi: 10.1017/S0022112065001660.

W. Myint, S. Hosokawa, and A. Tomiyama. Shapes of single drops rising through stagnant liquids. *Journal of Fluid Science and Technology*, 2(1):184–195, 2007. doi: 10.1299/jfst.2.184.

Y. Nakahara and A. Tomiyama. Shapes and rising velocities of single bubbles in vertical pipes. *Transactions of the Japan Society of Mechanical Engineers, Series B*, 69(685):2002–2009, 2003. in Japanese.

W.F. Noh and P. Woodward. Slic (simple line interface calculation). In *Lecture Notes in Physics*, volume 24, pages 330–340. Springer, 1976.

T. Okawa, T. Tanaka, I. Kataoka, and M. Mori. Temperature effect on single bubble rise characteristics in stagnant distilled water. *International Journal of Heat and Mass Transfer*, 46:903–913, 2003. doi: 10.1016/S0017-9310(02)00344-0.

S. Popinet. An accurate adaptive solver for surface-tension-driven interfacial flows. *Journal of Computational Physics*, 228:5838–5866, 2009.

M. Rastello, J.L. Marié, and M. Lance. Drag and lift forces on clean spherical and ellipsoidal bubbles in a solid-body rotating flow. *Journal of Fluid Mechanics*, 682:434–459, 2011. doi: 10.1017/jfm.2011.240.

P. Rollbusch, M. Bothe, M. Becker, M. Ludwig, M. Grünewald, M. Schlüter, and R. Franke. Bubble columns operated under industrially relevant conditions – current understanding of design parameters. *Chemical Engineering Science*, 126:660–678, 2015. ISSN 0009-2509. doi: https://doi.org/10.1016/j.ces.2014.11.061.

M.E. Rosti, F. De Vita., and L. Brandt. Numerical simulations of emulsions in shear flows. *Acta Mechanica*, 230:667–682, 2019.

W. Rybczynski. On the translatory motion of a fluid sphere in a viscous medium. *Bulletin International de l'Académie des Sciences de Cracovie*, 40:1735, 1911.

R. Scardovelli and S. Zaleski. Direct numerical simulation of free-surface and interfacial flow. *Annual Review of Fluid Mechanics*, 31:567–603, 1999. doi: 10.1146/annurev.fluid.31.1.567.

Y.T. Shah, B.G. Kelkar, S.P. Godbole, and W.D. Deckwer. Design parameters estimations for bubble column reactors. *AIChE Journal*, 28(3):353–379, May 1982. doi: 10.1002/aic.690280302.

G.B. Stokes. On the effect of the internal friction of fluids on the motion of pendulums. *Transactions of the Cambridge Philosophical Society*, 9:8–106, 1851.

K. Sugihara, T. Sanada, M. Shirota, and M. Watanabe. Behavior of single rising bubbles in superpurified water. *Kagaku Kogaku Ronbunshu*, 33(5):402–408, 2007.

T. Tadaki and S. Maeda. On the shape and velocity of single air bubbles rising in various liquids. *Chemical Engineering*, 25(4):254–264, 1961.

A. Tomiyama, I. Kataoka, I. Zun, and T. Sakaguchi. Drag coefficients of single bubbles under normal and micro gravity conditions. *JSME International Journal Series B*, 41(2), 1998.

G. Tryggvason, A. Esmaeeli, J. Lu, and S. Biswas. Direct numerical simulations of gas/liquid multiphase flows. *Fluid Dynamics Research*, 38(9):660–681, 2006. doi: 10.1016/j.fluiddyn.2005.09.003.

S. Uno and R.C. Kintner. Effect of walls on the motion of solid spheres in liquids. *AIChE Journal*, 2(3):420–425, 1956.

G.B. Wallis. *One-dimensional Two-phase Flow*. McGraw-Hill, New York, 1969.

R.M. Wellek, L.K. Agrawal, and A.H.P. Skelland. Shape of liquid drops moving in liquid media. *AIChE Journal*, 12(5):854–862, 1966.

F. Xiao, Y. Honma, and T. Kono. A simple algebraic interface capturing scheme using hyperbolic tangent function. *International Journal for Numerical Methods in Fluids*, 48(9):1023–1040, 2005.

D.L. Youngs. Time-dependent multi-material flow with large fluid distortion. In K. W. Morton and M. J. Baines, editors, *Numerical Methods for Fluid Dynamics*, pages 273–285. Academic Press, New York, 1982.

A. Appendix A

* Indicates oscillating cases, for which $E = E_{mean}$ and $BDF = BDF_{mean}$.
- Indicates bubbles undergoing breakup.

Eo	**Mo**	**Re**				**E**				**BDF**			
Eo	log_{10}Mo	χ=0.167	χ=0.25	χ=0.5	χ=0.667	χ=0.167	χ=0.25	χ=0.5	χ=0.667	χ=0.167	χ=0.25	χ=0.5	χ=0.667
0.01	-11.0	5.349e+00	4.593e+00	1.619e+00	5.514e-01	1.00	1.00	1.00	1.00	1.00	1.00	1.00	1.00
0.01	-9.4	1.072e+00	8.319e-01	2.510e-01	1.776e-01	1.00	1.00	1.00	1.00	1.00	1.00	1.00	1.00
0.01	-8.4	3.534e-01	2.723e-01	8.563e-02	7.985e-02	1.00	1.00	1.00	1.00	1.00	1.00	1.00	1.00
0.01	-7.3	1.052e-01	7.751e-02	2.507e-02	2.200e-02	1.00	0.96	0.96	0.96	1.00	1.00	1.00	1.00
0.01	-4.9	7.435e-03	5.004e-03	1.589e-03	1.342e-03	1.00	1.00	0.96	0.96	1.00	1.00	1.00	1.00
0.03	-11.0	2.583e+01	2.424e+01	1.067e+01	2.701e+00	0.96	1.00	1.00	0.96	1.00	1.00	1.00	1.00
0.03	-9.4	6.655e+00	5.846e+00	1.882e+00	1.033e+00	1.00	1.00	1.00	0.96	1.00	1.00	1.00	1.00
0.03	-8.0	1.528e+00	1.337e+00	3.891e-01	2.692e-01	1.00	1.00	1.00	0.96	1.00	1.00	1.00	1.00
0.03	-7.0	5.596e-01	4.337e-01	1.205e-01	1.033e-01	1.00	1.00	1.00	0.96	1.00	1.00	1.00	1.00
0.03	-5.0	5.697e-02	4.784e-02	1.200e-02	6.799e-03	1.00	1.00	0.96	0.96	1.00	1.00	1.00	1.00
0.03	-3.9	1.903e-02	1.291e-02	3.778e-03	7.477e-04	1.00	1.00	1.00	0.96	1.00	1.00	1.00	1.00
0.03	-3.0	6.710e-03	4.573e-03	1.429e-03	4.047e-04	1.00	1.00	1.00	0.96	1.00	1.00	1.00	1.01
0.10	-11.0	1.319e+02	1.270e+02	7.759e+01	1.819e+01	0.96	0.96	1.00	0.96	1.01	1.01	1.01	1.00
0.10	-9.4	3.666e+01	3.480e+01	1.824e+01	3.526e+00	0.96	1.00	1.00	0.96	1.00	1.00	1.01	1.00
0.10	-8.0	1.077e+01	9.926e+00	3.978e+00	6.523e-01	1.00	1.00	1.00	0.96	1.00	1.00	1.00	1.00
0.10	-6.6	2.711e+00	2.302e+00	7.821e-01	3.140e-01	1.00	1.00	0.96	0.96	1.00	1.00	1.00	1.00
0.10	-5.5	8.310e-01	6.867e-01	2.304e-01	7.708e-02	1.00	1.00	1.00	0.96	1.00	1.00	1.00	1.00
0.10	-3.0	4.448e-02	3.966e-02	1.427e-02	2.636e-03	1.00	1.00	0.96	0.96	1.00	1.00	1.00	1.00
0.10	-2.0	1.530e-02	1.283e-02	5.406e-03	7.145e-04	1.00	1.00	1.00	0.96	1.00	1.00	1.00	1.01
0.10	-3.9	1.505e-01	1.208e-01	4.225e-02	8.898e-03	1.00	1.00	0.96	0.96	1.00	1.00	1.00	1.00
0.30	-11.0	4.261e+02	4.157e+02	2.962e+02	1.232e+02	0.86	0.86	0.93	0.93	1.05	1.07	1.05	1.03
0.30	-9.4	1.400e+02	1.358e+02	9.111e+01	3.197e+01	0.93	0.96	0.96	0.96	1.03	1.04	1.04	0.98
0.30	-8.0	4.435e+01	4.261e+01	2.569e+01	7.252e+00	0.96	0.96	1.00	0.96	1.00	1.01	1.04	1.00
0.30	-4.9	2.324e+00	2.005e+00	8.064e-01	2.680e-01	0.96	1.00	1.00	0.96	1.00	1.00	1.02	1.00
0.30	-3.0	2.733e-01	2.298e-01	9.337e-02	3.485e-02	1.00	1.00	0.96	0.96	1.00	1.00	1.00	1.00
0.30	-2.0	8.769e-02	7.379e-02	3.318e-02	1.115e-02	1.00	1.00	1.00	0.96	1.00	1.00	1.00	1.00
0.30	-0.6	1.759e-02	1.494e-02	6.752e-03	8.945e-04	1.00	1.00	1.00	0.96	1.00	1.00	1.00	1.01
0.59	-5.5	1.073e+01	1.011e+01	5.131e+00	1.576e+00	1.00	1.00	1.00	0.96	1.00	1.00	1.01	0.97
1.00	-11.0	9.040e+02	8.872e+02	6.679e+02	3.766e+02	0.67	0.70	0.76	0.86	1.06	1.08	1.02	1.04
1.00	-9.4	3.528e+02	3.412e+02	2.585e+02	1.364e+02	0.68	0.72	0.79	0.89	1.18	1.10	1.10	1.06
1.00	-8.0	1.448e+02	1.400e+02	1.013e+02	4.863e+01	0.79	0.79	0.83	0.93	1.05	1.05	1.06	1.03

Eo	**Mo**	**Re**				**E**				**BDF**			
Eo	log_{10}Mo	$\chi=0.167$	$\chi=0.25$	$\chi=0.5$	$\chi=0.667$	$\chi=0.167$	$\chi=0.25$	$\chi=0.5$	$\chi=0.667$	$\chi=0.167$	$\chi=0.25$	$\chi=0.5$	$\chi=0.667$
1.00	-7.3	8.718e+01	8.463e+01	5.884e+01	2.584e+01	0.83	0.83	0.93	1.00	1.02	1.06	1.02	0.97
1.00	-6.6	4.972e+01	4.797e+01	3.187e+01	1.236e+01	0.83	0.86	0.93	0.96	1.03	1.03	1.03	0.98
1.00	-3.0	1.664e+00	1.438e+00	6.542e-01	2.385e-01	1.00	1.00	1.00	0.96	1.00	1.00	1.03	1.00
1.00	-1.3	2.485e-01	2.114e-01	9.832e-02	3.608e-02	1.00	1.00	1.00	1.00	1.00	1.00	1.00	1.00
1.00	0.3	3.782e-02	3.278e-02	1.553e-02	3.519e-03	1.00	1.00	1.00	0.96	1.00	1.00	1.00	1.01
1.66	-1.3	5.304e-01	4.534e-01	2.138e-01	7.937e-02	1.00	1.00	1.00	0.96	1.00	1.00	1.00	1.00
2.84	1.0	8.553e-02	7.335e-02	3.520e-02	1.325e-02	1.00	1.00	1.00	0.93	1.00	1.00	1.00	1.00
3.00	-11.0	1.256e+03	1.155e+03	9.505e+02	4.942e+02	0.67	0.69	0.69	0.86	1.07	1.05	1.04	1.02
3.00	-9.4	5.905e+02	5.561e+02	3.629e+02	2.368e+02	0.65	0.62	0.72	0.82	1.04	1.06	1.05	1.05
3.00	-8.0	2.696e+02	2.607e+02	1.936e+02	1.131e+02	0.55	0.58	0.65	0.76	1.10	1.10	1.07	1.04
3.00	-7.3	1.782e+02	1.709e+02	1.242e+02	7.156e+01	0.55	0.61	0.61	0.79	1.09	1.09	1.07	1.07
3.00	-6.6	1.144e+02	1.103e+02	7.900e+01	4.383e+01	0.61	0.61	0.68	0.82	1.08	1.07	1.06	1.04
3.00	-3.0	7.119e+00	6.560e+00	3.460e+00	1.323e+00	0.93	0.96	0.96	1.00	1.00	1.00	1.02	0.96
3.00	2.0	2.857e-02	2.434e-02	1.179e-02	4.501e-03	1.00	1.00	1.00	0.96	1.00	1.00	1.00	1.00
3.00	3.0	9.034e-03	7.716e-03	3.737e-03	7.144e-04	1.00	1.00	1.00	0.96	1.00	1.00	1.00	1.02
3.08	-2.0	2.748e+00	2.433e+00	1.193e+00	4.606e-01	0.96	1.00	0.96	0.93	1.00	1.00	1.01	1.00
3.50	0.3	2.506e-01	2.169e-01	1.043e-01	3.989e-02	1.00	1.00	1.00	0.96	1.00	1.00	1.00	1.00
3.57	-5.5	6.399e+01	6.197e+01	4.321e+01	2.238e+01	0.65	0.65	0.76	0.89	1.10	1.06	1.12	1.02
4.02	-3.9	2.182e+01	2.079e+01	1.308e+01	5.712e+00	0.76	0.76	0.83	1.00	1.02	1.02	1.04	0.98
8.66	-0.6	2.581e+00	2.288e+00	1.174e+00	5.147e-01	0.86	0.93	1.00	0.93	1.00	1.00	1.04	1.02
10.00	-11.0	2.508e+03	2.432e+03	1.664e+03	1.125e+03	0.41	0.39	0.45	0.59	1.26	1.29	1.18	1.09
10.00	-9.4	1.045e+03	9.751e+02	6.887e+02	4.475e+02	0.40	0.41	0.45	0.57	1.33	1.31	1.16	1.04
10.00	-8.0	4.866e+02	4.578e+02	2.754e+02	2.153e+02	0.44	0.45	0.50	0.55	1.27	1.28	1.15	1.07
10.00	-7.3	3.013e+02	2.862e+02	2.072e+02	1.343e+02	0.50	0.45	0.48	0.63	1.21	1.20	1.12	1.07
10.00	-6.6	2.127e+02	2.038e+02	1.344e+02	8.746e+01	0.40	0.45	0.50	0.60	1.26	1.10	1.11	1.06
10.00	-5.5	1.149e+02	1.075e+02	7.367e+01	4.557e+01	0.40	0.40	0.48	0.63	1.21	1.20	1.17	1.05
10.00	-3.9	4.234e+01	4.032e+01	2.704e+01	1.534e+01	0.46	0.46	0.58	0.79	1.08	1.14	1.02	1.03
10.00	-3.0	2.226e+01	2.118e+01	1.383e+01	7.429e+00	0.55	0.55	0.72	0.93	1.06	1.06	1.07	1.01
10.00	-2.0	1.052e+01	9.821e+00	5.948e+00	2.847e+00	0.65	0.68	0.83	0.96	1.03	1.02	1.02	0.97
10.00	2.0	1.742e-01	1.489e-01	7.405e-02	3.242e-02	1.00	1.00	0.96	0.90	1.00	1.00	1.00	1.00
10.00	3.0	5.543e-02	4.730e-02	2.354e-02	1.024e-02	0.96	1.00	1.00	0.93	1.00	1.00	1.00	1.00

Eo	**Mo**	**Re**				**E**				**BDF**			
Eo	log_{10}Mo	$\chi=0.167$	$\chi=0.25$	$\chi=0.5$	$\chi=0.667$	$\chi=0.167$	$\chi=0.25$	$\chi=0.5$	$\chi=0.667$	$\chi=0.167$	$\chi=0.25$	$\chi=0.5$	$\chi=0.667$
10.00	4.0	1.744e-02	1.489e-02	7.279e-03	2.703e-03	1.00	1.00	1.00	0.96	1.00	1.00	1.00	1.00
10.50	1.0	6.000e-01	5.137e-01	2.597e-01	1.162e-01	1.00	1.00	0.96	0.90	1.00	1.00	1.00	1.01
20.52	1.0	1.515e+00	1.327e+00	7.253e-01	3.706e-01	0.83	0.93	1.00	0.83	1.00	1.00	1.01	0.96
29.46	-0.6	9.461e+00	8.846e+00	5.859e+00	3.578e+00	0.52	0.52	0.79	0.89	1.10	1.09	1.10	1.02
30.00	-11.0	3.875e+03	3.432e+03	2.484e+03	2.398e+03	-	-	-	-	-	-	-	-
30.00	-9.4	1.356e+03	1.322e+03	8.686e+02	9.406e+02	-	-	-	-	-	-	-	-
30.00	-8.0	4.357e+02	5.629e+02	4.129e+02	4.562e+02	-	-	-	-	-	-	-	-
30.00	-5.5	1.317e+02	1.887e+02	1.030e+02	9.824e+01	-	-	-	-	-	-	-	-
30.00	-3.9	9.387e+01	8.751e+01	5.254e+01	3.705e+01	-	-	-	-	-	-	-	-
30.00	-2.0	2.451e+01	2.310e+01	1.646e+01	1.072e+01	0.35	0.35	0.54	0.69	1.31	1.22	1.06	1.03
30.00	2.0	8.526e-01	7.382e-01	4.086e-01	2.327e-01	0.93	0.93	0.89	0.75	1.00	1.01	1.02	1.05
30.00	3.0	2.850e-01	2.436e-01	1.317e-01	7.493e-02	1.00	0.96	0.89	0.77	1.00	1.00	1.00	1.02
30.00	4.0	9.106e-02	7.783e-02	4.183e-02	2.365e-02	1.00	1.00	0.86	0.75	1.00	1.00	1.00	1.04
30.00	5.0	2.878e-02	2.457e-02	1.324e-02	5.371e-03	1.00	1.00	0.89	0.93	1.00	1.00	1.00	1.01
30.00	6.0	9.099e-03	7.736e-03	3.870e-03	1.028e-03	1.00	1.00	1.00	0.96	1.01	1.01	1.00	1.05
41.36	1.0	3.570e+00	3.239e+00	1.998e+00	1.252e+00	0.72	0.72	0.96	0.77	1.03	1.03	1.03	1.03
100.00	2.0	3.897e+00	3.561e+00	2.282e+00	1.286e+00	skir	skir	skir	skir	1.09	1.08	1.09	1.03
100.00	4.0	5.291e-01	4.572e-01	2.651e-01	1.656e-01	0.93	0.96	0.86	skir	1.00	1.02	1.02	1.09
100.00	5.0	1.728e-01	1.485e-01	8.477e-02	5.239e-02	0.96	1.00	0.83	skir	1.00	1.01	1.02	1.10
100.00	6.0	5.535e-02	4.746e-02	2.688e-02	1.671e-02	1.00	1.00	0.83	skir	1.00	1.00	1.02	1.09
100.00	7.0	1.742e-02	1.502e-02	8.484e-03	4.097e-03	0.96	1.00	0.83	0.83	1.00	1.00	1.02	1.02
300.00	2.0	1.083e+01	1.044e+01	7.815e+00	5.413e+00	skir	skir	skir	skir	2.10	1.87	1.34	1.31
300.00	4.0	2.317e+00	2.075e+00	1.248e+00	7.922e-01	skir	skir	skir	skir	1.06	1.12	1.09	1.16
300.00	5.0	8.431e-01	7.379e-01	4.311e-01	2.594e-01	skir	skir	skir	skir	1.05	1.02	1.05	1.12
300.00	6.0	2.812e-01	2.432e-01	1.404e-01	8.679e-02	skir	skir	skir	skir	1.01	1.01	1.05	1.23
300.00	7.0	9.050e-02	7.666e-02	4.476e-02	2.824e-02	0.96	skir	skir	skir	1.00	1.03	1.04	1.09
300.00	8.0	2.879e-02	2.470e-02	1.411e-02	7.360e-03	1.00	0.96	skir	skir	1.00	1.01	1.06	1.04
1000.00	3.0	1.427e+01	1.407e+01	1.043e+01	7.603e+00	skir	skir	skir	skir	2.84	2.50	2.08	1.70
1000.00	5.0	3.848e+00	3.520e+00	2.230e+00	1.235e+00	skir	skir	skir	skir	1.25	1.23	1.16	1.24
1000.00	7.0	5.273e-01	4.564e-01	2.394e-01	1.599e-01	skir	skir	skir	skir	1.07	1.07	1.06	1.17
1000.00	8.0	1.732e-01	1.443e-01	8.615e-02	3.106e-02	0.96	skir	skir	skir	1.00	1.03	1.06	1.02

B. Appendix B

* Indicates oscillating cases, for which $E = E_{mean}$ and $BDF = BDF_{mean}$.
- Indicates bubbles undergoing breakup.

Eo	log_{10}Mo	Re	E	BDF	Eo	log_{10}Mo	Re	E	BDF
0.01	-11.0	5.597e+00	1.00	1.00	3.50	0.3	2.772e-01	1.00	1.00
0.01	-9.4	1.201e+00	1.00	1.00	3.57	-5.5	6.654e+01	0.65	1.08
0.01	-8.4	4.055e-01	1.00	1.00	4.02	-3.9	2.218e+01	0.76	1.03
0.01	-7.3	1.177e-01	1.00	1.00	8.66	-0.6	2.719e+00	0.83	1.00
0.01	-4.9	8.542e-03	1.00	1.00	10.00	-11.0	2.578e+03	0.37*	1.31*
0.03	-11.0	2.625e+01	1.00	1.00	10.00	-9.4	9.293e+02	0.43*	1.35*
0.03	-9.4	7.069e+00	1.00	1.00	10.00	-8.0	4.812e+02	0.57*	1.26*
0.03	-8.0	1.861e+00	1.00	1.00	10.00	-7.3	3.126e+02	0.47	1.23
0.03	-7.0	6.338e-01	1.00	1.00	10.00	-6.6	2.173e+02	0.41	1.27
0.03	-5.0	6.524e-02	0.96	1.00	10.00	-5.5	1.196e+02	0.40	1.22
0.03	-3.9	1.993e-02	1.00	1.00	10.00	-3.9	4.391e+01	0.46	1.08
0.03	-3.0	7.042e-03	1.00	1.00	10.00	-3.0	2.271e+01	0.55	1.08
0.10	-11.0	1.506e+02	1.00	1.01	10.00	-2.0	1.073e+01	0.68	1.03
0.10	-9.4	3.760e+01	1.00	1.00	10.00	2.0	1.888e-01	0.96	1.00
0.10	-8.0	1.103e+01	0.96	1.00	10.00	3.0	6.018e-02	1.00	1.00
0.10	-6.6	2.882e+00	1.00	1.00	10.00	4.0	1.906e-02	1.00	1.00
0.10	-5.5	9.144e-01	1.00	1.00	10.50	1.0	6.477e-01	0.96	1.00
0.10	-3.0	5.335e-02	1.00	1.00	20.52	1.0	1.611e+00	0.83	1.00
0.10	-2.0	1.719e-02	1.00	1.00	29.46	-0.6	9.691e+00	0.48	1.11
0.10	-3.9	1.636e-01	1.00	1.00	30.00	-11.0	-	-	-
0.30	-11.0	4.720e+02	0.83	1.09	30.00	-9.4	-	-	-
0.30	-9.4	1.534e+02	0.93	1.05	30.00	-8.0	-	-	-
0.30	-8.0	4.687e+01	0.96	1.02	30.00	-5.5	-	-	-
0.30	-4.9	2.303e+00	1.00	1.00	30.00	-3.9	-	-	-
0.30	-3.0	2.813e-01	1.00	1.00	30.00	-2.0	2.486e+01	0.35	1.32
0.30	-2.0	9.616e-02	1.00	1.00	30.00	2.0	9.168e-01	0.93	1.00
0.30	-0.6	1.985e-02	1.00	1.00	30.00	3.0	3.061e-01	0.96	1.00
0.59	-5.5	1.104e+01	0.96	1.00	30.00	4.0	9.856e-02	0.96	1.00
1.00	-11.0	9.961e+02	0.70	1.03	30.00	5.0	3.135e-02	0.96	1.00
1.00	-9.4	3.926e+02	0.70	1.09	30.00	6.0	9.948e-03	1.00	1.00
1.00	-8.0	1.563e+02	0.76	1.15	41.36	1.0	3.703e+00	0.65	1.05
1.00	-7.3	9.393e+01	0.83	1.09	100.00	2.0	4.026e+00	skir	1.13
1.00	-6.6	5.233e+01	0.83	1.05	100.00	4.0	5.716e-01	0.93	1.00
1.00	-3.0	1.783e+00	1.00	1.00	100.00	5.0	1.879e-01	0.96	1.00
1.00	-1.3	2.710e-01	1.00	1.00	100.00	6.0	6.026e-02	1.00	1.00
1.00	0.3	4.217e-02	1.00	1.00	100.00	7.0	1.896e-02	0.96	1.00
1.66	-1.3	5.783e-01	1.00	1.00	300.00	2.0	1.117e+01	skir	2.10
2.84	1.0	9.375e-02	1.00	1.00	300.00	4.0	2.421e+00	skir	1.15
3.00	-11.0	1.386e+03	0.68	1.05	300.00	5.0	9.046e-01	skir	1.04
3.00	-9.4	5.527e+02	0.70	1.04	300.00	6.0	3.049e-01	0.96	1.00
3.00	-8.0	2.774e+02	0.56	1.09	300.00	7.0	9.864e-02	1.00	1.00
3.00	-7.3	1.854e+02	0.58	1.10	300.00	8.0	3.136e-02	1.00	1.00
3.00	-6.6	1.236e+02	0.58	1.09	1000.00	3.0	1.488e+01	skir	2.73
3.00	-3.0	7.301e+00	0.86	1.00	1000.00	5.0	3.957e+00	skir	1.33
3.00	2.0	3.123e-02	1.00	1.00	1000.00	7.0	5.706e-01	skir	1.02
3.00	3.0	9.871e-03	1.00	1.00	1000.00	8.0	1.879e-01	0.96	1.00
3.08	-2.0	2.903e+00	0.96	1.00					

Abstract in lingua italiana

La comprensione dei flussi bifase gas-liquido con bolle richiede una descrizione accurata della dinamica della singola bolla, in termini di velocità terminale, forma e area interfacciale. Il presente lavoro amplia lo studio condotto da Belleri, 2025 sulla risalita di una singola bolla in dominio non confinato, per esaminare l'influenza delle pareti sulla dinamica. Mediante il codice proprietario *Fujin*, sviluppato presso l'Okinawa Institute of Science and Technology, sono state condotte simulazioni DNS utilizzando il metodo Volume of Fluid (VOF), al fine di studiare i meccanismi fisici alla base del fenomeno e costruire un ampio database numerico. Le simulazioni coprono un ampio intervallo dei numeri di Morton ed Eötvös ($10^{-11} \leq Mo \leq 10^{8}$ and $10^{-2} \leq Eo \leq 10^{3}$) e diversi rapporti di confinamento ($\chi = 0.167$, 0.25, 0.5 and 0.667). I risultati mostrano che il confinamento induce una riduzione della velocità terminale della bolla, più pronunciata per bassi valori del numero di Eötvös e alti valori del numero di Morton. Si propone una correlazione che esprime tale riduzione in funzione dei numeri di Eötvös e Morton e del rapporto di confinamento. La presenza di pareti favorisce, inoltre, un allungamento longitudinale della bolla e un'anticipazione dell'insorgenza di bolle con "gonna" (configurazioni dimpled e skirted), con tendenze dipendenti dalle proprietà del fluido. Sono introdotte nuove correlazioni per il rapporto di forma della bolla e per il fattore di deformazione della bolla, che estendono le formulazioni per il caso non confinato includendo il rapporto di confinamento. La riduzione della velocità indotta dalle pareti è interpretata dal punto di vista fisico mostrando come il confinamento localizzi la dissipazione viscosa nella regione di gap tra bolla e parete, modificando il bilancio di potenza che governa la risalita e dunque conducendo a un nuovo punto di equilibrio.

Parole chiave: Bolla, Confinamento, VOF, Velocità terminale, Rapporto di forma, Area interfacciale

Acknowledgements

The author gratefully acknowledges the Complex Fluids and Flows Unit at Okinawa Institute of Science and Technology (OIST) for hosting him during a six-month research internship, and the Scientific Computing and Data Analysis section of the Research Support Division at OIST for providing computational resources.